TECHNISCHE UNIVERSITÄT WIEN
Vienna University of Technology

DIPLOMARBEIT

Experimental Validation of the Ripple Filter Effect of Lung Tissue Equivalent Materials in a Proton Beam

zur Erlangung des akademischen Grades

Diplom-Ingenieur

im Rahmen des Masterstudiums
Technische Physik
an der Technischen Universität Wien

ausgeführt am
Atominstitut
Fakultät für Physik
Technische Universität Wien

in Zusammenarbeit mit der
Universitätsklinik für Strahlentherapie
Medizinische Universität Wien und MedAustron

durch
Andreas Hranek, BSc
Matrikelnummer 00928976

Betreuer: **Univ.-Prof. DI. Dr. Dietmar Georg**
Mitwirkung: **Mag. Barbara Knäusl, PhD**

Wien, October 21, 2019

Unterschrift Student

Unterschrift Betreuer

Abstract

Ion beam therapy offers the advantage of an increased dose deposition at the end of the particle's range (Bragg peak (BP)), which results in a sharp fall off behind the tumour and potentially allows a better sparing of the surrounding healthy tissue. Lung cancer could profit essentially from particle therapy by decreasing the dose to the ipsilateral lung and avoiding the contralateral lung completely. Besides the challenges of respiration motion, lung tissue has a very heterogeneous texture, which poses difficulties for available dose calculation algorithms. This varying density affects the stopping power along the particles path and results in a spreading of the BP. Clinically used dose calculation algorithms implemented in treatment planning systems (TPS) are based on the stopping power information received from a patient's CT images. Their resolution is limited to about 1 mm while the size of inhomogeneities for lung tissue is in the sub-millimetre region. The aim of this thesis was to investigate the proton beam in heterogeneous materials mimicking lung tissue, quantify its properties, try to predict the effect on the beam and further compare them to Monte Carlo dose calculations of the TPS.

Materials, which were suitable as lung substitute, were chosen based on their structure and density, namely cork (2 with different densities), konjac sponge, floral foam, pumice and balsawood, all available with different thickness. Additionally, lung tissue equivalent plates (CIRS, USA) were included representing the correct atomic composition but not representing the realistic texture of the heterogeneities. Integral depth dose (IDD) of a proton beam with 97.4 MeV and 148.2 MeV were measured in a water phantom (MP3-PL, PTW, Germany) with a reference ionisation chamber (Type 34080, PTW, Germany) and a field ionisation BP chamber (Type 34070, PTW, Germany). The investigated materials were positioned in front of the entrance window of the water phantom and their IDDs compared to reference measurements without additional material in the beam path. From the dose curves different points of interest were derived, the so called R_X, which is the range at $X\%$ of the height of the peak. Those were the necessary basic information for calculations of the water equivalent thickness (WET) and σ (derived from the FWHM of the BP). Based on the correlation between different thickness of lung equivalent plates results for WET and σ were normalised to the same width (in mm) and thickness (in g/cm^2) of materials for comparison purposes. The heterogeneity of the materials was quantified by the modulation power. A correlation between the Hounsfield units (HU) and heterogeneities was investigated by comparing σ to the HU spectrum of a material. Furthermore, measurements were compared to Monte Carlo (v4.1) dose calculation in RayStation 6.99 (RaySearch, Sweden). Lateral profiles were measured, where instead of the field ionisation chamber a microDiamond chamber (Type 60019, PTW, Germany) was used, to investigate the effects of inhomogeneities

in transversal beam direction. The depths at which the profiles were acquired were depending on the material's R_{80} for comparability between the materials.

The investigations of the WET normalised to the same thickness (1 g/cm^2) yielded an average WET of all materials excluding the pumice of 9.8 mm. The values for the lung tissue equivalent plates, the cork samples and the konjac sponge were within 5 %, about 6 % for the balsawood and the floral foam and about 10 % for the pumice. The findings of the WET were independent of the heterogeneity of the material in terms of range shifting but affected by the thickness determination of the material. In case of pumice the deviation of the WET from the average value was caused by the atomic composition. The derived values of the modulation power as quantity of the material heterogeneity were between 0.09 and 0.13 mm for the lung tissue equivalent plates, between 0.61 and 0.66 mm for the cork with higher density, 0.80 mm for the cork with lower density, 0.12 mm for the balsawood, 0.68 mm for the floral foam, 1.06 mm for the konjac sponge and 1.15 mm for the pumice. For the heterogeneous materials with a modulation power larger than 0.13 mm the heterogeneous contribution to the spreading of the BP was two to three times larger than the homogeneous contribution. This heterogeneity was correlated to the variation of HU within the material via a square root function, under the precondition that the inhomogeneities were distinguishable in the CT. This was the case for the cork samples, the konjac sponge and by lacking of inhomogeneity for the lung tissue equivalent plates. Neither the WET nor σ were found to be energy dependent at clinically relevant energies. Further did the inhomogeneities not effect the lateral spreading of the beam within the measured accuracy. The comparison of measurements to Monte Carlo dose simulation in RayStation yielded that the treatment planning system was capable of predicting the range of homogeneous and inhomogeneous materials equally well. However, it was not capable to consider the Bragg peak spreading caused by the material heterogeneity and lead to an underestimation. Future research aims at verifying will be to verify the results of lung substitutes for real lung tissue and quantify its modulation power to allow corrections of the TPS dose calculation.

Kurzfassung

In der Ionentherapie wird die Eigenschaft von geladenen Teilchen ausgenutzt am Ende ihrer Reichweite den größten Teil ihrer Dosis an ihre Umgebung abzugeben (Bragg Peak (BP)). Das führt zu einem steilen Dosisabfall hinter dem bestrahlten Tumor und folglich einer geringeren Strahlenbelastung für das umliegende, gesunde Gewebe. Besonders die Behandlung von Lungentumoren kann von dem Dosisverhalten der Teilchenstrahlung profitieren, indem der ipsilaterale Lungenflügel geschont und die Bestrahlung des contralateralen Lungenflügel vollständig vermieden werden kann. Neben der Herausforderung der Atembewegungen, hat Lungengewebe eine sehr heterogene Struktur, welche Auswirkungen auf die deponierte Dosis hat. Die Variation der Dichte im Gewebe beeinflusst das Stoßbremsvermögen entlang der Teilchenpfade was zu einem Aufweiten des Bragg Peaks führt. Klinische Dosisberechnungen in Behandlungsplanungssystemen basieren auf Informationen des Stoßbremsvermögens, welche aus den CT Bildern des Patienten berechnet werden. Die Auflösung kann dabei allerdings nach momentanem Stand nicht höher als 1 Millimeter sein, wobei die Inhomogenitäten im Lungengewebe im Submillimeterbereich liegen. Ziel dieser Arbeit war es das Verhalten des Protonenstrahls in heterogenen Materialien, die Lungengewebe ähneln, zu untersuchen, dessen Eigenschaften zu quantifizieren, zu versuchen diese vorherzusagen und weiters die zugehörige Dosisberechnung des Planungssystem mit den experimentellen Messungen zu vergleichen.

Die Materialen, welche Ähnlichkeit zu Lungengewebe haben sollten, wurden nach den Kriterien ihrer Dichte und ihrer Struktur ausgewählt. Dies waren zwei verschiedene Korkarten mit unterschiedlicher Dichte, ein Konjakschwamm, ein Blumensteckschwamm, ein Bimsstein und ein Stück Balsaholz. Zusätzlich wurden lungenäquivalente Platten (CIRS, USA) verwendet, deren Komposition der von echtem Lungengewebe entspricht, allerdings die Inhomogenität nicht repräsentiert. Integrale Tiefendosiskurven (IDD) wurden mit einem Protonenstrahl bei 97.4 MeV and 148.2 MeV in einem Wasserphantom (MP3-PL, PTW, Deutschland) mittels Referenzionisationskammer (Typ 34070, PTW, Deutschland) and Feldionisationskammer (Typ 34080, PTW, Deutschland) gemessen. Die untersuchten Materialen wurde vor dem Wasserphantom positioniert und ihre gemessenen IDDs zu den Referenzmessungen im Wasser ohne zusätzliches Material im Strahlengang verglichen. Verschiedene Punkte entlang der Dosiskurven wurden ermittelt, die üblicherweise als R_X angegeben werden, welche die Reichweite im Wasser relative zur Höhe (X %) des Bragg Peak Maximums darstellen. Diese Punkte bildeten die Grundlage zur Berechnung der WET (wasseräquivalente Dicke) and σ (abgeleitet vom FWHM des BP). Basierend auf der Korrelation von WET und σ von unterschiedlichen Dicken der lungenäquivalenten Platten wurden die Ergebnisse zur Vergleichbarkeit auf einheitliche

Dicken (in mm) und Flächendichten (in g/cm^2) normiert. Die Heterogenität wurde als Modulation Power bestimmt. Nach einer Korrelation zwischen den Hounsfield Units (HU) und den Inhomogenitäten im Material wurde gesucht indem σ mit dem HU Spektrum im Material in Beziehung gesetzt wurde. Außerdem wurden die Messergebnisse zu Monte Carlo Dosisberechnungen (v4.1) in RayStation 6.99 (RaySearch, Schweden) verglichen. Weiters wurden auch laterale Dosisprofile gemessen. Zur Messung dieser Profile wurde anstelle der Feldionisationskammer ein microDiamond Detektor (Typ 60019, PTW, Deutschland) verwendet. Ziel war es den Effekt der Inhomogenitäten im Material in transversaler Ausbreitungsrichtung des Teilchenstrahls zu untersuchen. Die jeweiligen Tiefen, in welcher die Profile gemessen wurde, waren abhängig vom jeweiligen R_{80} Wertes des Materials.

Eine Untersuchung der WET normalisiert zur gleichen Flächendichte (1 g/cm^2) ergab, dass die Lungenplatten, die Korkproben und der Konjakschwamm innerhalb einer 5 % Schwankung um den Mittelwert von $9,8$ mm lag. Für Balsaholz und Blumensteckschwamm lag sie bei etwa 6 % und etwa bei 10 % für den Bimsstein. Die WET zeigte keine Abhängigkeit von der Inhomogenität des Materials, abseits der Tatsache, dass durch die Materialinhomogenitäten die Bestimmung der Flächendichte erschwert wurde. Die größere Abweichung des Bimssteines wurde auf seine atomare Komposition zurückgeführt. Für die Modulation Power wurden Werte zwischen $0,09$ bis $0,13$ mm für die Lungenplatten gemessen, zwischen $0,61$ und $0,66$ mm für die Korkstücke mit höherer Dichte, $0,80$ mm für die Korkprobe mit geringerer Dichte, $0,12$ mm für das Balsaholz, $0,68$ mm für den Blumensteckschwamm, $1,06$ mm für den Konjakschwamm und $1,15$ mm für den Bimsstein. Für Materialen deren Modulation Power größer war als $0,13$ mm wurde festgestellt, dass der inhomogene Beitrag zur Aufweitung des BP σ zwei- bis dreimal größer was als der homogene Beitrag. Die Heterogenität im Material wurde mittels einer Wurzelfunktion zur Größe der Variation der HU im Material korreliert. Die Voraussetzung war allerdings, dass die Inhomogenitäten im CT abgebildet werden konnten. Dies war der Fall für die verschiedenen Korkproben, den Konjakschwamm und durch das Fehlen von Inhomogenität auch für die Lungenplatten. Weder für die WET noch für σ wurde eine Energieabhängigkeit für die klinisch relevanten, getesteten Energien festgestellt. Weiters führten die Inhomogenitäten auch zu keinen Effekten in lateraler Richtung im Rahmen der Messgenauigkeit. Der Vergleich der Messdaten zu den Monte Carlo Dosisberechnungen ergab, dass das Planungssystem die Reichweite des Strahls durchs Material für die homogenen sowie die inhomogenen Proben gleich gut voraussagen konnte. Allerdings wurden die inhomogenen Effekte in der Aufweitung des Bragg Peaks nicht adäquat berücksichtigt und führten durchgehend für alle getesteten Materialien zu einer Unterschätzung der Aufweitung. Ziel künftiger Arbeiten sollte es sein, die Ergebnisse der Lungensubstitute mit denen von echtem Lungengewebe zu vergleichen, die Modulation Power zu berechnen, die als Korrekturfaktoren für Dosisberechnungsalgorithmen verwendet werden könnten.

Contents

1. Introduction

1.1. Overview on Cancer Therapy

Cancer is a long known and studied disease during human history. The name cancer is Latin and derives from the Greek word karcinos used by Hippocrates which means crab. It was thought that a spreading tumour resembles a crab. Over the years a large number of different treatment techniques have been developed. Today the three standard pillars of cancer therapy are surgery, radiation oncology and chemotherapy. [1]

Surgery is a long existing, effective technique and is documented to have already been used over 2000 years ago. It is still the most frequently used option in cancer management. With improvements in medicine and surgical equipment the capabilities have come from simple amputations to high precision operations. [2]

Radiation therapy was first to be applied only months after the discovery of X-rays by Wilhelm Röntgen in 1895. In 1896 Leopold Freund performed in Vienna the first X-ray treatment. The patient was a 5 year old girl with a skin disease leading to vast hair growth on the back (naevus pigmentosus piliferous). The treatment lead to side effects, especially in the region where the two photon fields overlapped, but were documented with 77 year follow up. To that time, the understanding of radiation and its effect were low and the first treatment successes poor. With better knowledge and continuous research, different types of radiations were discovered and applied in therapy. First used were photons in form of X-rays then neutrons, electrons, protons, alpha particles and heavier ions as therapy options. Also particles such as pions were studied for clinical applications.
Today the radiotherapeutic options are not only sorted by radiation type but also by delivering technique. The three delivering techniques are sealed source (brachytherapy), unsealed source (radionuclide therapy) and external beam radiotherapy. [3, 4]

The third conventional cancer treatment is chemotherapy. It started evolving in the late first half of the twentieth century. Special drugs are injected into the patient which attach themselves to the tumour. The advantage of this therapy is that it allows to treat tumours which can not be localised well or have developed metastases. The type and effect of the applied drugs are very diverse. Also their delivery to the tumour is different, some require markers, heat or light to be able to enter the tumour walls. [2]

Most of the time a combination of different treatment techniques is applied for better

targeting, side-effect reduction or adaptations necessary during the treatment period. Not all treatments are capable of curing the patient (curative treatment), in some cases the aim of the treatment is an improvement of quality of life (palliative treatment). [4]

1.2. Dose Delivery Techniques in Radiation Therapy

Unsealed Source Therapy

This technique is applied in nuclear medicine and not in radiation oncology, but was added for the sake of completeness. In this treatment approach a radioactive nuclide (radionuclide therapy) is inserted into the patient directly either by injection or ingestion. The nuclide is attached to a carrier molecule which targets the tumour. The decaying isotopes deposit their energy in the surrounding tissue, mainly to the tumour. Therefore, particles which emit short ranged radiation are preferred such as β-particles, Auger and conversion electrons and α-particles. In contrast to X- and γ-radiation, their ranges are considerable short and their impact on healthy tissue small. Furthermore, the half life of the isotope should be relative short to not be present in the patient body for a too long time and cause undesired side-effects. The dose deposition is continuous and decreases over time, contrary to the fractionated radiation used by other treatment techniques. Special molecules, which carry the radioactive nuclide, are used to target different tumour types. The targets of the molecules can be within the cell (intracellular) to directly hit the DNA or on the tumour cells surface attached via hormones, peptides or antibodies. The targets can also be proximately close to the tumour cells (extracellular), where the radioactive nuclides target radiolabelled cells, or are injected directly at the tumours position. [5]
Aside from the treatment itself, radioisotopes are also used for organ screening and tumour detection in nuclear medicine. In those cases isotopes with a much lower dose are chosen. Their decay products have a higher range so they can leave the body and are possible to detect. [2]

Sealed Source Therapy

In brachytherapy a sealed source is placed close to the tumour. The sealed source can be inserted into the body of the patient or placed close to the skin, depending on the treated target. The dose is either delivered continuously over a longer time period of months or year at low dose rates or temporary at high dose rates with multiple fractions during the treatment period. Examples of continuous delivery at lower dose rate are implants, called seeds, which are injected permanent into the patient, while the source is decaying, or plaques mounted to the body of the patient, for example the eye. Fractionated delivery is applied via applicators which are inserted into the patient and contain a highly radioactive source, that is removed after the treatment period.
Typical brachytherapy sources are photon emitters, but there are also β-emitters and even a few cases where neutron emitting sources are used. [2, 5, 6]

Teletherapy

In external beam radiotherapy, also called teletherapy, the radiation source is far away from the patient and the created beam is directed toward the tumour. A large number of different particles can be used for the beam, ranging from few keV X-ray photons to oxygen ions but also particles such as pions are possible.

Photons are typically obtained from radioactive sources or created with an X-ray machine or a Linear accelerator (LINAC), where accelerated electrons strike a thick target and Bremsstrahlung with a broad energy spectrum are produced. For clinical applications electron beams are mostly produced and accelerated by LINACs, while betatrons and microtrons are not used any longer.
Proton and neutron (produced when protons hit a target) beams can be produced in a cyclotron or a synchrotron, while heavier ion beams can only be produced by a synchrotron. The variety of available particle beams allows to treat tumours seated at different positions. The penetration depth depends on the particle type and the energy. An overview of dose deposition at different depths for different particles is given in Figure 1.1. The different particle beams do not only have different dose depositions but also different intensities, field sizes and radiobiological effectivenesses (explained later). Depending on the tumour and the surrounding tissue different approached are suitable. [3, 5, 7]

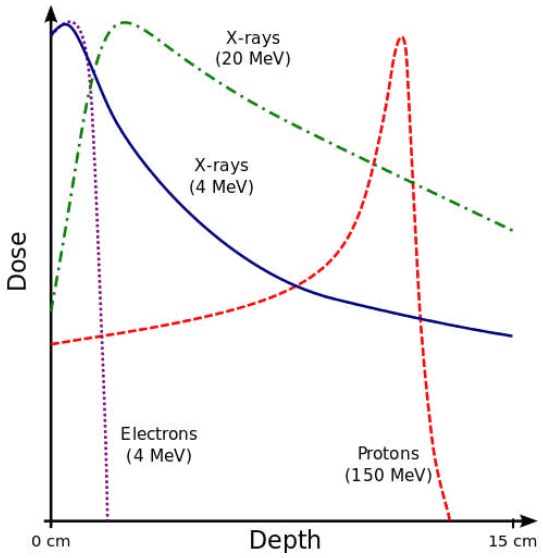

Figure 1.1.: Normalised depth dose curves of different particles in water (figure from [8])

1.3. Treatment Workflow

For patients diagnosed with cancer an appropriate therapy is chosen by a team of oncologists depending on the type, position, size and stage of the tumour. Upon decision for a certain treatment in agreement with the patient, the therapeutic process can be roughly categorised into three stages: imaging, treatment planning and treatment delivery. In relevance for this thesis, the focus will be primary on the treatment workflow seen in ion beam therapy (IBT) as it can be very different from other cancer therapies. [5, 7, 9, 10]

Imaging

> "If you can't see it, you can't hit it, and if you can't hit it, you can't cure it." - Canadian physicist Harold E. Johns

This statement used by Johns, who was a pioneer in ^{60}Co-source teletherapy in the nineteen-fifties, is still valid today and has become even more important with the improving technologies in medical physics. Imaging is the precondition for treatment planning, a recurring necessity during treatment and essential in the treatment follow up. It is crucial to localise and characterise tumour and surrounding organs-at-risk (OAR) precisely for proper treatment. Images of the patient for identifying OARs and target volumes are: Computer tomography (CT), magnetic resonance imaging (MRI) and positron emission tomography (PET)

CT Computer tomography is the standard option for imaging as treatment plans are generated based on the density information provided by CT images. The patient is lying on a table while a rotatable X-ray beam traverses the patient and detectors are located opposite to the source. From the attenuation of the intensity of the photon flux the electron density along the beam path is reconstructed. By rotating the beam and the detector three dimensional images can be obtained with a slice thickness between 1 and 5 mm. The resulting CT voxels are then assigned to Hounsfield unit (HU). The value is a result of the attenuation of the photons and per definition is the HU of water equal to 0 and -1000 for air (see Equation 2.21).

MRI Magnetic resonance imaging, also MR tomography, does not use ionising radiation and, therefore, offers the advantage of not causing an additional dose burden to patients. MRI mostly uses signals from hydrogen nuclei, which is abundant in water and fat and comprises $50 - 70$ % of the patients body. A static magnetic field is applied which forbids metal parts on or inside the patients body. In the field, the spin of the protons is aligned parallel or anti-parallel to the field and results in a precession of the nuclei. By applying a magnetic pulse sequence transversal to the static field the orientation of the precession changes. The relaxation of the precession to its prior orientation creates a signal. The relaxation time depends on the tissue and is responsible for the contrast. The

soft tissue contrast is superior to CT. However, the visibility of bony structures is rather poor, because MRI usually focus on protons, therefore, only water and fat abundant materials are visible in the images.

PET In positron emission tomography a β^+-decaying isotope is injected into the patient. In the annihilation process of positron and electron two photons are created which propagate in opposing directions. The photons are detected by photomultiplier tubes. The isotope is inserted into the body with a biologically active molecule which gives information about the biochemical function of tissue rather than structure. This allows to identify metastasis, outlines of tumours and infected lymph nodes better than CT or MRI. PET scanners are commonly integrated into CT machines for more precise image fusion.

Aside from tumour localisation, the imaging technologies are important for the positioning of the patient. The position of the patient needs to be comfortable and reproducible during imaging and treatments. In reverse, the images are also used to reproduce the position the patient on a daily basis during the treatment course. To verify the position inside the treatment room planar X-ray radiography, cone beam computer tomography (CBCT) or ultrasound images are used.
In special cases where patient movements are inevitable, such as breathing, the motion needs to be tracked. [11, 12]

Planning

The treatment planning is performed either forward, where the beam shape and weight is defined and the resulting dose calculated, or "inverse", where a certain dose is prescribed and the required beam properties are calculated, the so called intensity modulated radiotherapy (IMRT). The dose prescription for the target depends on the diagnosis. The images acquired of the patient are used to identify the tumours and with help of a delineation software the targets and the OAR are contoured. The terminology of target volume is defined in the ICRU Report 50 [13] and 62 [14] and illustrated in Figure 1.2.

GTV Gross Tumour Volume: represents the primary tumour, which is visible in the CT.

CTV Clinical Target Volume: contains the GTV and additionally considers microscopic spreading of the tumour in the surrounding tissue

ITV Internal Target Volume: contains the CTV and adds internal margins which account for tumour movements and position uncertainties.

PTV Planning Target Volume: contains the ITV and takes external, safety margins into account which can be uncertainties of the beam and the patient position or other minor variations during treatment. It is designed to ensure that the CTV is treated with the prescribed dose in any case.

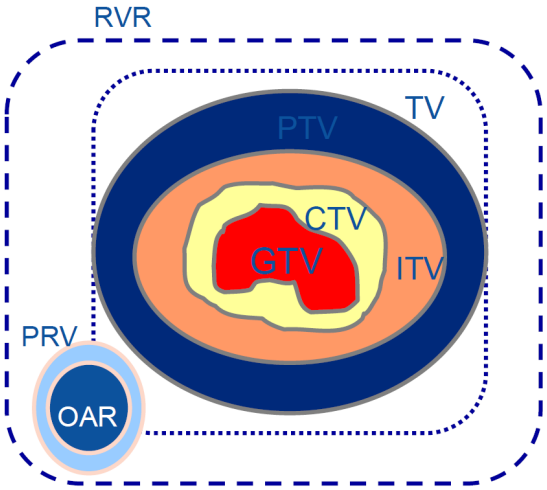

Figure 1.2.: Different treatment planning volumes as defined in the ICRU Reports 50 and 62 (figure from [14])

TV Treated Volume: is the volume that receives a certain dose level (isodose). For example, $D_{98\%} = 1$ Gy means that 98 % of the volume receive a dose of at least 1 Gy.

OAR Organ at Risk: is normal tissue, which is radio sensitive and should be exposed to as little radiation as possible. For all relevant OARs clinical goals are defined based on clinical data about radiation induced side effects which are taken into account in the treatment planning process.

PRV Planning Organ at Risk Volume: is the extended OAR volume which considers safety margins as the PTV does for the CTV.

RVR Remaining Volume at Risk: is as indicated by the name the region inside the external contours of the patient but excluding CTVs and OARs. This region needs to be considered to avoid undesired dose hot spots.

In cases where CTV and OAR are so close together that their planning volumes overlap ICRU Reports 78 and 83 give the recommendation that first the CTV must be covered, then the PRV spared and last the PTV covered. Further it is recommended that the dose delivered to the target should be uniform within -5 % to +7 %.
The algorithm to calculate the dose depends on the beam delivery system, in general the commonly used algorithms are: Ray trace, Pencil beam (PB), Monte Carlo (MC) and collapsed cone (in photon therapy). [3, 11]

Treatment

During treatment the patient is positioned in the treatment room in the same position as during the imaging process. Once the safety checks are finished and the position

verified, the prescribed treatment plan is loaded and the beam delivered. In IBT the beam is delivered either by passive scattering or active scanning (see Section 2.1). [15]

1.4. MedAustron

MedAustron is a centre for ion beam therapy in Wiener Neustadt, Austria, 50 km south of the capital city Vienna. The idea was developed as part of the Austron project in the nineties in the twentieth century in close collaboration with CERN, the Technical University Vienna and other central European countries. The construction work started in march 2011 and patients are treated since end of 2016 with protons.

MedAustron is a synchrotron-based facility, which is capable of accelerating protons to a velocity of 30 - 84 % of the speed of light. After acceleration the particles are extracted from the ring and distributed to one of the four irradiation rooms, three for clinical treatment and one for non-clinical research.

Currently proton beams between 60 and 250 MeV are available for treatment, which is equivalent to 3 to 38 cm range. For superficial tumours located at depth of less than 3 cm a range shifter is used further reduce the range For research 800 MeV proton beams are available and investigated for feasibility of proton CT imaging, which would be desired over X-ray CTs in IBT for easier determination of tissue specific stopping powers (see Section 2.2). The carbon beam commission phase for an energy range of 120 to 400 MeV/u is happening since August 2019.

MedAustron uses the pencil beam scanning technique for beam delivery. It also has a robotic system to move the treatment table with the patient with highest precision supported by a laser tracking system. It is the only ion beam therapy centre in Austria and offers the advantage of highly flexible and adaptive treatment plan customisations even for difficult treatment cases.

1.5. Motivation

Lung cancer is responsible for more than 20 % of all cancer related deaths in the EU-28 [16], 23 % in the United States [17] and around 29 % in eastern Asia [18]. In general, lung cancer is difficult to treat. Small cell lung cancer (SCLC) tends to spread which limits the use of surgery. The non small cell lung cancer (NSCLC) is rather localised and better suited for surgery, however, treatment usually requires the removing of parts of the lung. Aside from chemotherapy, radiation oncology provides an important tool for a combined treatment, particularly when surgery is not possible [2]. Aims to improve treatment are going on in all fields.

IBT profits from high dose deposition in the region of the Bragg peak while sparing healthy tissue in distant regions. For lung cancer, particle therapy helps by decreasing

the dose to the ipsilateral lung and avoiding the contralateral lung completely. However, two problems accompany the precision-sensitive target treatment: the respiratory motion and the tissue structure.
The respiratory motion leads to the largest uncertainties in the treatment of all kind of moving tumours, like lung, liver and pancreatic cancer. It needs to be countered by breath control, motion tracking and/or well-timed irradiation (gating [19]).
Nevertheless, especially for the treatment of lung cancer the uncertainties caused by tissue structure needs to be taken into account by careful investigating the tissue heterogeneities and consideration in the dose determination process.

In this thesis different lung substitutes were investigated, their properties quantified and the measurements with a proton beam were compared to MC based dose calculations. As shown by Taylor et. al. [20] dose calculation algorithms can not predict the dose correctly. One of the main reasons is that the fine structure of the lung tissue with alveoli diameters between $0.2 - 0.5$ mm and membranes and blood vessels down to µm ranges [21]. However, the CT resolution cannot be smaller than 1 mm and therefore a mean value within the resolution is obtained, which cannot display the effect on an ion beam correctly using the current methods. In Figure 1.3a the micrograph is shown and in contrast a CT image in Figure 1.3b. There the CT gives a rather homogeneous image, however, these heterogeneities shown in the micrograph have significant effects on the ion beam, especially the Bragg peak, and lead to an effect called ripple filter effect (see Section 2.3.1). By quantifying this effect it could be used to correct dose calculations.

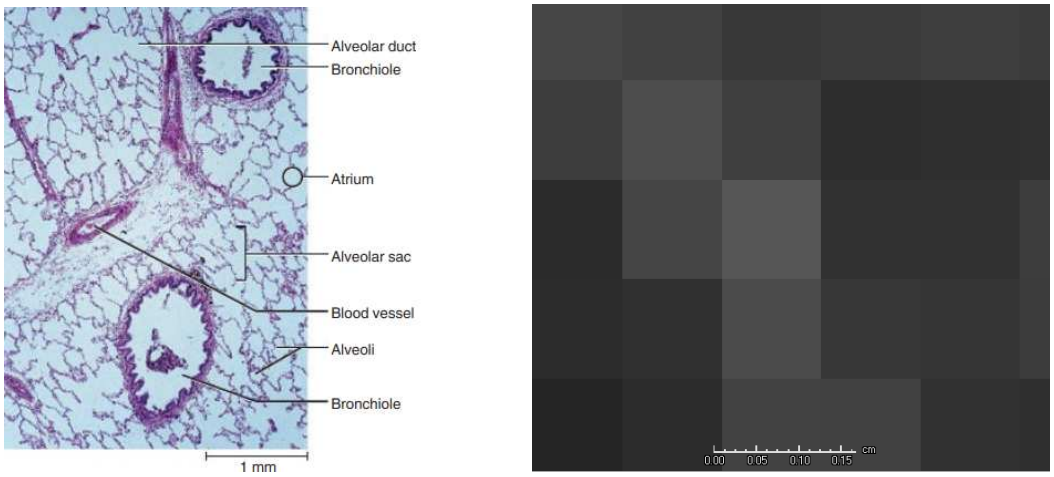

(a) Lung tissue under the microscope

(b) Lung tissue displayed in a CT

Figure 1.3.: Structure resolution of lung tissue of a micrograph (figure from [21]) compared to a CT image

2. Theoretical Concepts in Proton Radiotherapy

2.1. Particle Accelerators

Cyclotron

In the centre of the accelerator protons are injected from an ion source. In a strong static magnetic field B the particles start circulating inside two hollow semicircular cylinders, called dees ("D"-shaped). The dees are electrodes, which create a high frequent alternating electric field in the gap between them, which accelerates the protons and lead to a spiral trajectory due to the increasing centrifugal force. When the particles pass from one dee to the other, the electric field switches direction to continue accelerating the particles. The frequency of field needs to match the circulation time of the particles in the magnetic field according to Equation 2.1, which is derived from the Lorentz force equals the centrifugal force.

$$f = \frac{v}{2\pi r} = \frac{Q \cdot B}{2\pi m} \tag{2.1}$$

Due to the independence of the frequency f from the radius r for constant magnetic fields B, new protons can be injected after every full circle and create a continuous particle beam. At the outer edge of the dees the particles are extracted by deflection. The protons have a fixed energy determined by the constant magnetic field and radius at the end of the circulation. To lower their energy and to treat more superficial targets energy degraders are necessary. Those range shifters produce undesired secondary radiation, mostly neutrons, and reduce the particle fluence at low energies. Cyclotrons have the advantage of steadily injecting new protons into the machine and producing a continuous proton beam.
Classic cyclotrons are only usable at non-relativistic velocities, because at relativistic energies the mass of the protons increases. For relativistic velocities necessary for treatment advanced machines such as synchrocyclotrons or isochronous cyclotrons are required. [3, 5]

Linear Accelerator

LINACs are not used as stand alone technology in IBT, but are used as pre-accelerator for the synchrotron. Below the principles are explained for use in photon and electron usage, which is slightly different than for protons.
In a LINAC a modulator creates high voltage pulses which are simultaneously delivered

to an electron gun and a microwave generator (either a magnetron or a klystron). The electron gun produces electrons in a heated cathode and injects them into the accelerator tube (accelerator waveguide). The microwave source produces well timed microwave pulses, which accelerates the electrons analogous to a surfer riding a wave. At the end of the tube the electrons are ejected and are guided with magnets toward the target. With a scattering foil the narrow electron beam (3 mm) is widened and with help of collimators brought to the desired shape.
Alternatively the LINAC can be operated as an X-ray source. In this mode, instead of a scattering foil, a target material with high atomic number (typically tungsten) is placed in the electron beam path. The electrons get fully absorbed and instead an X-ray beam is created via Bremsstrahlung. The intensity of the new beam profile is then uniformed with a flattening filter. [5, 15]

Synchrotron

From an electron cyclotron resonance (ECR) ion source a particle stream is obtained. It is brought to shape and striped from remaining electrons with a radio frequency quadrupole (RFQ), which accelerates the beam to approximately 400 keV/u. Instead of electrons, the ions are then injected into a LINAC and are pre-accelerated to around 7 MeV (at MedAustron). From the LINAC the ions are injected into an accelerator ring with fixed radius. Dipole electromagnets accelerate the particles, while quadrupole electromagnets keep the beam focused. The magnets switched on with synchronous frequency to the circulating ions. The frequency increases with every circulation as the particles speed up. The ions are accelerated until the desired energy is reached. Then the ions are extracted over a period of a few seconds and the package, called spill, is guided to the treatment room, where it is delivered either by active scanning or passive scattering (see Section 1.3). Once all particles are extracted from the accelerator ring or to deliver a different beam energy, new ions need to be accelerated in the synchrotron to the desired energy. This results in a dead time between the spills and the beam is not delivered constantly over time, but like a square wave function, called pulsed beam. In IBT, beams usually start by delivering the highest energy first and then decrease the energy. [3, 15]

Cyclotrons and synchrotrons have one of two modalities to deliver the beam. One is passive scattering and one is active scanning. [15]

passive In the passive scattering beam delivery system a single beam is spread with a range shifter wheel or a ridge filter and dual scattering foils. The edges of the enlarged beam are trimmed to a sharp dose fall off by a collimator and a uniform field is remaining. A range compensator in shape of the PTV projection, which needs to be manufactured before the treatment, is used to shape the beam to deliver the maximum dose to the target volume and spare the surrounding OARs.

active In the pencil beam scanning method a narrow beam is deflected by magnets to

target multiple spots covering the PTV. For three dimensional PTV coverage the penetration depth of the beam is modified by changing the energy or by using range shifters. Those are additional material in the beam path and shorten the penetration depth of the beam particles in the tissue. Heavier particles than protons require additionally a ripple filter (see Section 2.3.1).

On one hand, passive scattering requires a PTV-shaped compensator which needs to be manufactured before the treatment and delivers a higher dose outside the PTV, on the other hand, pencil beam scanning is more prone to position changes and overall more complex. The methods are too complex to be used both at the same facility and therefore only one is in use. However, pencil beam scanning is the more advanced technology and today almost only active scanning facilities are built.

2.2. Interaction of Protons with Matter

Charged particle beams such as proton beams and are part of directly ionising radiation. When traversing matter, a charged particle undergoes different interaction mechanisms. Those include Coulomb interactions with the atomic electrons or nucleus, nuclear reactions and Bremsstrahlung. The charged particle loses energy in most interactions it undergoes. The stopping power S_{tot} is defined as the mean energy loss $\mathrm{d}E$ per unit path length $\mathrm{d}x$ can be separated into three contributions: The energy loss is defined per path length $\mathrm{d}x$ and called stopping power S_{tot}.

$$S_{\text{tot}} = \left(\frac{\mathrm{d}E}{\mathrm{d}x}\right)_{\text{tot}} = \left(\frac{\mathrm{d}E}{\mathrm{d}x}\right)_{\text{el}} + \left(\frac{\mathrm{d}E}{\mathrm{d}x}\right)_{\text{rad}} + \left(\frac{\mathrm{d}E}{\mathrm{d}x}\right)_{\text{nuc}} \tag{2.2}$$

In IBT the radiation losses S_{rad} negligible small and most energy is lost via collisions. Clinical proton beams typically operate with energies up to 250 MeV while radiation losses become relevant at kinetic energies in the GeV-region [22]. However, for light charged particles, such as electrons, radiation losses are important. A detailed derivation is given by Podgorsak [23].

Three types of collisions are relevant for protons [24]: inelastic scattering with atomic electrons, elastic scattering with the nucleus and non-elastic nuclear reactions.

Inelastic Coulomb scattering with atomic electrons is the dominant contributor to the electronic collision stopping power S_{el} [25]. In the classic approach [26] derived by Niels Bohr, a heavy charged particle transfers a momentum Δp via Coulomb force F to the electron.

$$\Delta p = \frac{1}{v}\int F_{\perp}\mathrm{d}x = \frac{e}{v}\int E_{\perp}\mathrm{d}x \tag{2.3}$$

From Gauss' law (Equation 2.4) the electric field $E_{\perp}$ is derived and

$$\int_A \vec{\mathbf{E}} * \mathrm{d}\vec{\mathbf{A}} = 2\pi b \int E_{\perp}\mathrm{d}x = \frac{Q}{\epsilon_0} = \frac{Z_p e}{\epsilon_0} \tag{2.4}$$

Equation 2.3 is rewritten to

$$\Delta p = \frac{1}{2\pi\epsilon_0}\frac{Z_p e^2}{vb}. \tag{2.5}$$

The transferred momentum Δp is determined by the charge of the traversing particle $Z_p \cdot e$, its velocity v and the distance b to the interacting electron. The total energy loss is given as the integral over the transferred kinetic energy with an electron density n_e in a cylindrical volume with propagation direction x of the particle and radial distance to the electrons b.

$$\mathrm{d}E = -\left(\int_{b_{\min}}^{b_{\max}} \frac{\Delta p^2}{2m_e} n_e 2\pi b \ \mathrm{d}b\right)\mathrm{d}x \tag{2.6}$$

The collision stopping power is then of the following form:

$$\frac{\mathrm{d}E}{\mathrm{d}x} = -\frac{Z_p^2 e^4 n_e}{4\pi\epsilon_0^2 v^2 m_e}\ln\left(\frac{b_{\max}}{b_{\min}}\right) \tag{2.7}$$

In the classical limit, the maximal energy in a single collision is transferred at minimal distance $b_{\min}$ and at maximal distance $b_{\max}$ the minimal energy transfer is the mean ionisation energy I of the electron. The classic Bohr stopping power is then:

$$\frac{\mathrm{d}E}{\mathrm{d}x} = -\frac{Z_p^2 e^4 n_e}{2\pi\epsilon_0^2 v^2 m_e}\ln\left(\frac{2m_e v^2}{I}\right) \tag{2.8}$$

Hans Bethe and Felix Bloch later improved equation 2.8 by applying quantum mechanical and relativistic physics [23]. Bethe treated distant (soft) collisions and close (hard) collisions separately. In general, for soft collisions the energy transfer was smaller than the ionisation energy I and larger for the hard collisions. The Bethe mass collision stopping power is expressed in Equation 2.9. In the approximation of $I = Z_t \cdot 10$ eV this is also known as Bethe-Bloch equation, although, literature is not consistent in designation.

$$S_{\mathrm{el}} = S_{\mathrm{el}}^{\mathrm{soft}} + S_{\mathrm{el}}^{\mathrm{hard}} = -\frac{1}{\rho}\frac{\mathrm{d}E}{\mathrm{d}x} = \frac{Z_p^2 Z_t e^4 N_{\mathrm{A}}}{4\pi A_t \epsilon_0^2 m_e c^2 \beta^2}\left(\ln\left(\frac{2m_e c^2}{I}\right) - \ln\left(\frac{\beta^2}{1-\beta^2}\right) - \beta^2\right) \tag{2.9}$$

The Bethe formula 2.9 was later extended by Ugo Fano since the Born approximation used by Bethe does not hold in the low energetic limit. Fano introduced two corrections: the shell corrections and the polarisation correction. The shell correction accounts for atomic electrons with a velocity similar to the traversing particles. This leads to an overestimation of the ionisation energy as the electrons no longer get excited. The density or polarisation correction describes the polarisation of the medium during soft collisions. Thereby the stopping power is reduced.

The mass collision stopping power with the above corrections is given as

$$S_{\mathrm{el}} = \frac{Z_p^2 Z_t e^4 N_{\mathrm{A}}}{4\pi A_t \epsilon_0^2 m_e c^2 \beta^2}\left(\ln\left(\frac{2m_e c^2}{I}\right) - \ln\left(\frac{\beta^2}{1-\beta^2}\right) - \beta^2 - \frac{C}{Z_t} - \frac{\delta}{2}\right). \tag{2.10}$$

Another form of energy loss comes from inelastic interactions with the nucleus. The incident proton undergoes either large angle scattering or a nuclear reaction. The effect on the particles are significant but is less likely than electron collisions and not considered in the stopping power[1]. Usually it is given as the planar fluence Φ reduction of a particle beam traversing through a medium:

$$\Phi(t) = \Phi_0 e^{-\frac{t}{s}}, \tag{2.11}$$

where t is the thickness of the traversed medium and s the corresponding free path length of the incident particles. In clinical proton beams, the fluence reduction of a proton beam in water is about 1 % per cm [5].

The third collision type relevant for protons is elastic nuclear scattering (Rutherford scattering) and called nuclear stopping power S_{nuc} [25, 27]. The scatter angles are small and energy transfer is only relevant at low energies (< 1 MeV for protons), which allows Equation 2.10 to be a valid approximation in IBT.
Many small angle scatterings, called multiple Coulomb scattering (MCS), lead to a lateral spreading of the beam. This spreading is defined similar to the stopping power as scattering power T with the mean scattering angle θ [24].

$$T = \frac{\mathrm{d}\theta^2}{\mathrm{d}x} \tag{2.12}$$

The sum of all energy losses displayed against the penetration depth in a material gives the Bragg curve, as shown in red in Figure 1.1. The Bragg curve describes the energy loss of a particle beam at a certain penetration depth and the maximum is called Bragg peak (BP), which is an important characteristic used in IBT. It results from an increased ionisation in the medium as the charged particles in the beam slow down. The deposed energy at a certain depth is also referred to as Bragg curve, though, the energy loss of a particle is not identical to the deposed energy. The secondary particles created in the proton beam can have a different range and depose energy elsewhere. In this thesis the dose maximum will be referred as Bragg peak.

2.3. Bragg Peak Spreading

From the proton BP in Figure 1.1 (red line) it can be seen that the fall-off after the maximum is not sharp, but steadily falling. Note that the shape of the red curve in Figure 1.1 is only valid for protons. Heavier ions have a steeper rise and fall-off, followed by a slowly decreasing dose region. This is an effect of the beam particles breaking apart

[1] not to confuse with S_{nuc}

and fragments continue to travel in beam direction, therefore called fragmentation tail.

The steady fall-off after the BP maximum is because of two effects with similar results, the range and the energy straggling [28], which results in a spreading of the BP. Due to interactions in the traversed medium the particles lose different amounts of energies in each interaction, which lead to different ranges when the particles lost all their energy, this is the energy straggling. The range straggling assumes a similar situation where monoenergetic particles get deflected due to collisions (MCS) resulting in different ranges for the same path lengths. In first order approximation the statistical distribution of the straggling is assumed to be Gaussian.

For thick absorbers relative to the range of the particle, but not very thick [28], the number of interactions N is in the limit of $N \rightarrow \infty$, Bohr approximated the stragglings of non-relativistic particles as a Gaussian distribution.

$$\sigma_0^2 = \frac{Z_t e^4 N_\mathrm{A}}{4\pi\epsilon_0^2 A_t} \cdot W \cdot \rho \tag{2.13}$$

In the relativistic extension Equation 2.13 becomes

$$\sigma^2 = \frac{1 - \frac{\beta^2}{2}}{1 - \beta^2} \cdot \frac{Z_t e^4 N_\mathrm{A}}{4\pi\epsilon_0^2 A_t} \cdot W \cdot \rho. \tag{2.14}$$

Different models of straggling were proposed by L. Landau or P. V. Vavilov, which were discussed for example by Newhauser and Zhang [24] or Leo [28].
Equation 2.14 is suitable for the description of the spreading of the BP caused by additional homogeneous material in the beam path, which is currently used by the treatment planning system RayStation. For the full BP spreading in water Equation 2.13 is not valid as a small energy loss was assumed.

Due to interactions with mater the Bragg peak does not only spread in beam direction but the beam also spreads in lateral direction. This is essentially a consequence of MCS as described above. The lateral distribution is approximately a Gaussian and given in Equation 2.15. A detailed derivation is given by Leo [28].

$$P(\theta_x)\mathrm{d}\theta_x = \frac{1}{\sqrt{2\pi\,\langle\theta_x^2\rangle}} e^{-\frac{\theta_x^2}{2\langle\theta_x^2\rangle}}\ \mathrm{d}\theta_x \tag{2.15}$$

In Figure 2.1 the spreading of the BP and the beam are displayed for protons in water for different energies.

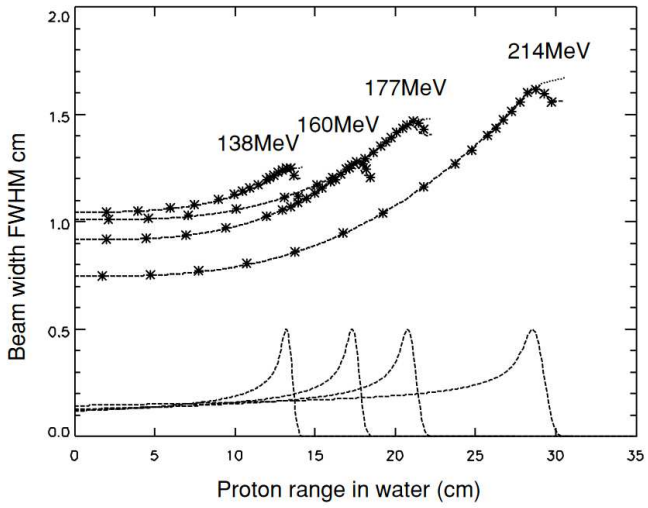

Figure 2.1.: Lateral and longitudinal spreading of protons in water for different energies (figure from [29])

2.3.1. Spread Out Bragg Peak and Ripple Filter Effect

In IBT a single Bragg peak is usually not sufficient to cover the tumour in beam direction. For longitudinal coverage, multiple beam energies with different penetration depths and BP positions are used. The energies are chosen in such a way that the accumulated dose forms a plateau in the tumour region, also referred to as spread out Bragg peak (SOBP). Figure 2.2 shows two effects of a SOBP: an increase of the dose deposition before the maximum region and a wobbling in the plateau region.

The effect of a raised initial dose is handled by delivering the dose from more than one direction. The wobbling in the SOBP can not be avoided as particle energies can not be applied continuously. This requires proper choice of energy spacing in the treatment planning process. For particles heavier than protons, such as carbon ions, is additionally a so called ripple filter (RiFi) required. Those consist of a thin base plate and parallel triangle-shaped stripes. When a beam passes through the triangle shapes it experience a straggling effect which widens the BP and smears out the wobbling. This is necessary as heavier particles have a narrower and sharper BP, due to a larger gradient of the stopping power at low energies, which results in faster energy loss close to the end of the particles range.

A similar effect to the one of a RiFi occurs naturally in tissue, especially lung and bone tissue, and is therefore called ripple filter effect. Tissue heterogeneities lead to locally varying atomic composition and density. The former effect is small compared to the latter, nonetheless both affect the stopping power [5]. Particles passing through an inhomogeneous material experience individual straggling from the different stopping

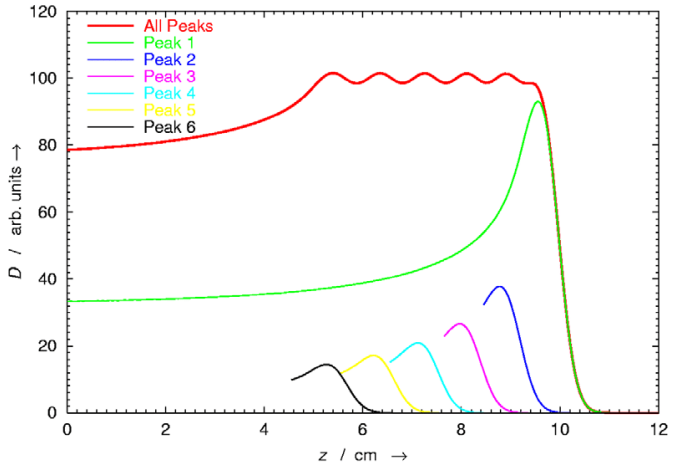

Figure 2.2.: Spread out Bragg peak by accumulation of multiple single Bragg peaks (figure from [24])

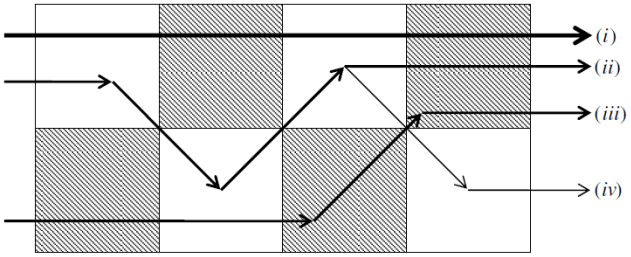

Figure 2.3.: Density heterogeneities experienced for particles along different paths (figure from [31])

powers along their paths, as illustrated in Figure 2.3. The consequence is that the individual particles have different ranges, respectively BP positions. The cumulated dose of Bragg curves of each particle then results in a spreading of the BP and a lower maximum, referred by Urie as degradation of the BP [30]. In lung tissue the density variation is formed by air filled alveoli (0.001 g/cm^3) and blood vessels and soft tissue (1.06 g/cm^3).

2.4. Dosimetric Aspects

The main quantity in radiation oncology is the absorbed dose D. It is defined as the absorbed mean energy imparted by ionising radiation per mass element dm with mass density ρ in units of Gray (1 Gy = 1 J/kg) [9].

$$D = \frac{\mathrm{d}\overline{E}}{\mathrm{d}m} = \frac{1}{\rho}\frac{\mathrm{d}\overline{E}}{\mathrm{d}V} \tag{2.16}$$

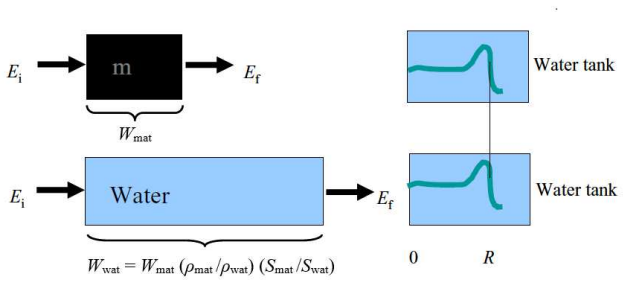

Figure 2.4.: Definition of water equivalent thickness for particles beams traversing a material and deposing their final energy in water (figure adapted from [33])

Dosimetric measurements are often conducted in water, since the density and the materials composition is comparable to human tissue [32]. It is common to convert measurements on other materials to water equivalent properties. A typical quantity in IBT is the water equivalent thickness (WET), which describes the penetration range of the particle beam in a material and is converted to a water equivalent range, which is approximated to:

$$t_{wat} = W_{wat} \cdot \rho_{wat} = \frac{W_{mat} \cdot \rho_{mat} \cdot S_{mat}}{S_{wat}} \tag{2.17}$$

where W is the width of the traversed material with a density ρ and a mass stopping power S [33]. A graphical display equivalent to Equation 2.17 is given in Figure 2.4. An equivalent material thickness means that the particle beam has the same range in the water tank. Analogue, a different range in the water tank gives the offset of the WET caused by the material. Ranges R are usually given as the penetration depth in water relative to the maximum of the BP, for example R_{80} is the range in water at 80 % of the peak height before (proximal) and after (distal) the BP maximum.

Note that in different literature, thickness t is used in units of g/cm^2 and cm. To avoid misunderstanding, in this thesis a width W is always given as a length and thickness t always as the product of density and width (called areal density [34]). An exception is made for the WET which will be used in units of length, however, since the density of water is assumed to be one it is equivalent to a thickness t.

The Bragg curves shown in the figures before (1.1, 2.1, 2.2) are usually displayed as a lateral dose as a function of depth, called integral depth dose (IDD). In this form, the whole energy deposition in a plane perpendicular to the penetration depth is given. Alternatively, the dose can be given along the central beam axis. However, it is easier to build large detectors than infinite small ones, which need to positioned exactly in the beam centre. In a field of multiple pencil beams, the observed dose with a small detector would correspond to an IDD again (reciprocity theorem). Therefore, IDDs are

commonly used to display the dose along the penetration depth. The actual dose at a certain depth and position is lower, because of the Gaussian shaped beam cross section and the lateral fluence of the beam.

2.5. Detectors

2.5.1. Ionisation Chamber

Incoming radiation leads to an ionisation in the gas filled cavity. The applied voltage to the electrodes of the detector leads to a charge separation of ions and electrons. The electric field is sufficient to prevent recombination of the created ions, while being insufficient to cause additional collision ionisation on the way to the electrodes (region B in Figure 2.5). By detecting the accumulated charge the mean deposed energy in the

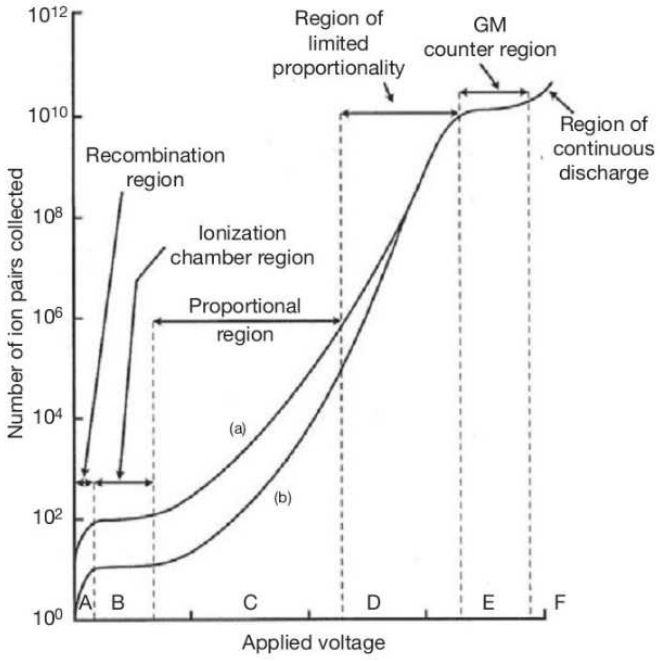

Figure 2.5.: Response of ionisation chambers to incident radiation for two different energies (figure from [7])

detector can be calculated. Two common types of ionisation chambers are: plane parallel and thimble chambers.
Plane parallel chambers have two parallel electrodes with a diameter in the range of a few cm and an effective gas volume for detection of 1 to hundreds of cm^3. In IBT the electrode plane is commonly perpendicular to the beam and the centres of the plane and beam aligned. Their design allows to detect dose in a large plane perpendicular to the beam direction and obtain IDD profiles.

Thimble, cylindrical like chambers have an outer cylindrical electrode with a round or pointed tip. The inner electrode is a thin cylinder along the centre of the outer electrode. Their active volume is typically between 0.01 and 1 cm^3. For measurement their orientation can be axial or radial to the beam direction. [7, 9]

2.5.2. Diode Detector

A semiconductor diode consists of two regions: one has an excess (n-doted) and one to have a lack of electrons (p-doted). The electrons drift to the p-doted side while the holes drift to the n-doted side. Due to the diffusion of electrons and holes the charges, which cannot move freely and is bound to a location, produce an electric field opposing the drift direction. An equilibrium and on the interface (p-n junction) a region without free charge carrier is formed (depletion area), which prevents electric current.
When operated as a detector ionising radiation ionises atoms and creates electron-hole pairs in the diode. The pairs diffuse into the depletion area and are swept across it due to the electric field. This current, which is created in reverse direction of the diode, is proportional to the radiation dose. In Figure 2.6 the current voltage diagram of a diode is shown. The detector operates in the third quadrant in the region before the breakdown.
A special type of diodes are Schottky diodes. Instead of two semiconducting regions, one of them is replaced by a metal (typically the p-doted). The depletion area is smaller and the diode reacts more sensitive to radiation. The microDiamond detector used for measurements in this thesis is one of those detectors. [7, 9, 35]

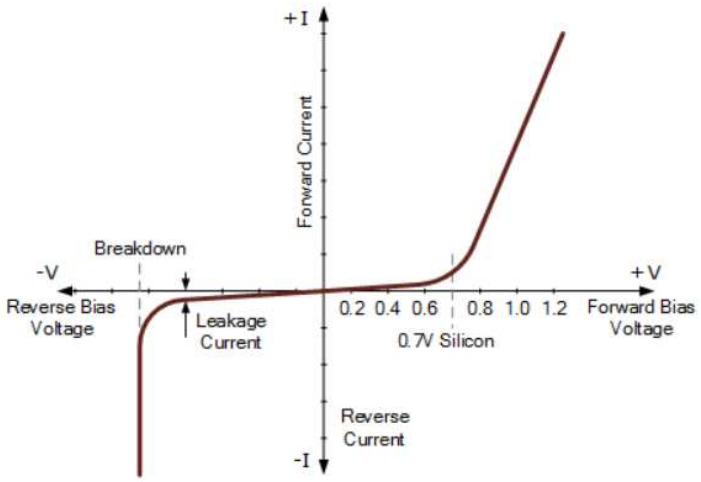

Figure 2.6.: Current-Voltage diagram of a diode (figure adapted from [36])

2.6. Effect of Ionising Radiation on Tissue

Ionising Radiation causes cell damages in tissue. The effects are divided into direct effects (deterministic) and latent effects (stochastic).
The damage dealt to the cell which consequently leads to its death are caused by direct damage to the DNA or indirectly by creating free radicals in proximity of the DNA. The types of DNA lesions (shown in Figure 2.7) result in different survival rates of the cell. Photons ionise atoms and produce radicals, which damage molecules around

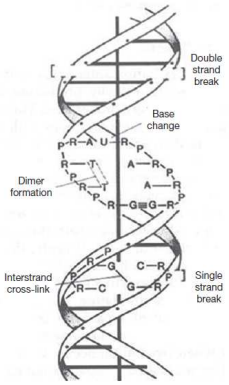

Figure 2.7.: Different lesions in the DNA caused by radiation (figure from [9])

it. The resulting lesions in the DNA are less severe than lesions created by charged particles, which cause more complex, difficult to repair lesions. The relative biologic effectiveness (RBE) is the ratio of dose deposited by a radiation with different beam quality yielding for the same survival rate of cells.

$$\mathrm{RBE} = \frac{\text{reference dose}}{\text{dose from investigated radiation}} \tag{2.18}$$

As reference dose historically 250 keV X-rays were used, whereas nowadays 1.3 MeV γ-rays from a ^{60}Co source are the standard [9]. For protons the RBE is clinically approximated to be constant and equal to $= 1.1$, despite it is known to vary over the beam range. Different effects such as the linear energy transfer (LET) and the abundance of molecular oxygen are relevant as well [5, 9, 37]. Moreover, the factor 1.1 is heavily discussed in the proton beam community [38]. In contrast to proton therapy, the RBE of carbon ions is so high and strongly varying with depth that a constant value does not suffice. Therefore, the most commonly used RBE models are the Japanese (modified) microdosimetric kinetic model (MKM) and the European local effect model (LEM) [38].

Compared to tumour cells, healthy tissue has a better recovery rate from radiation. This opens a (therapeutic) window, where the tumour control probability prevails the normal tissue complication probability, as shown in Figure 2.8. This effect is further utilised by applying dose to the patient in fractions (typically $1-2$ Gy) over an ongoing time period than all dose at once (typically $50-60$ Gy).

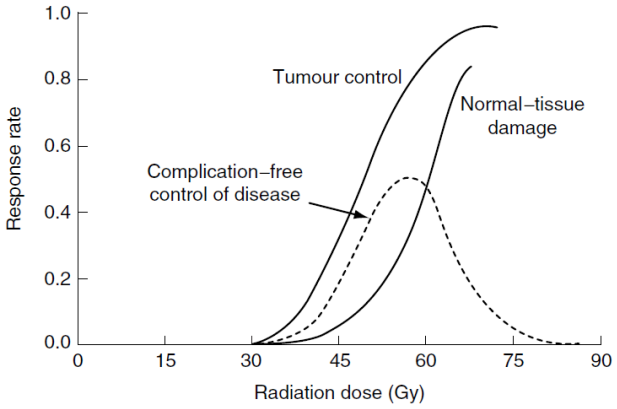

Figure 2.8.: Concept for complication-free tumour control (figure from [5])

2.7. CT Conversion

Treatment plans are created on basis of CT scans. As already mentioned, an $X-ray$ tube rotates around the patient with a synchronised-rotating detector on the opposite side. The photon beam is fanned out to cover a larger area. While rotating the table with the patient is moving to scan a larger volume of the patient. By traversing the patent, the initial intensity I_0 of photon beam is attenuated according to Beer's law (Equation 2.19). The photon attenuation is a result of the absorption and scattering of photons in matter.

$$I(x) = I_0 e^{-\mu x} \tag{2.19}$$

After a path length d the intensity $I(d)$ reaches the detector. As the linear attenuation coefficient μ is position dependent, it can be written as the sum over a defined number of discrete steps Δx. $I(d)$ then becomes

$$I(d) = I_0 e^{-\Delta x \cdot \sum \mu_i}. \tag{2.20}$$

In Figure 2.9 the principle is shown. The only unknown quantity are the μ_i and by super-positioning the different images an algorithm creates a matrix and assigns every voxel an attenuation value μ_i. Detailed information about image acquisition and reconstruction are given by Dance et. al. [9]. For easier handling of data the linear attenuation coefficients in the matrix are converted to HU according to Equation 2.21.

$$HU = 1000 \cdot \frac{\mu - \mu_{water}}{\mu_{water}} \tag{2.21}$$

In dependence of the CT scanner settings a HU voxel resolution between 1 to 5 mm is obtained.

Ion beam dose calculation requires the stopping power and, the HU value of each voxel

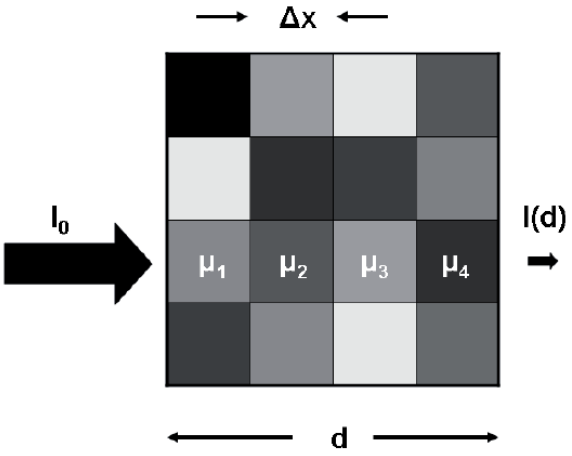

Figure 2.9.: Principle of assigning linear attenuation coefficients in a simplified matrix (figure from [9])

is then converted to a corresponding mass density based on a calibration table, where in-between values are linear interpolated. The mass densities to HU relations are typical values for different tissues [32], for example lung, muscle or bone, but also for metallic inserts. Each scanner and scanning protocol requires its own conversion table. The elemental composition and mean excitation energy needs to be additionally accounted for charged particles as it affects the mass stopping power of the ion beam. These additional values are assigned the same way as for the mass density to each CT voxel. The mass density, mean ionisation energy and elemental composition are used to recalibrate the material specific stopping power from the stopping power of water [32, 39].

2.8. Treatment Planning System

For dose calculation, a dose grid is set to the CT image which can be the same size as the CT grid or larger, typically ranging from 1 to 5 mm voxel size. Within each dose voxel the dose is calculated separately. The dose voxel takes the values of the CT voxels within and weights them depending on their volume fraction. For calculating the final dose per voxel different models can be used. In active scanning proton radiotherapy the PB and the MC algorithm are commonly used.

2.8.1. RayStation 7 Dose Calculation

2.8.1.1. Pencil Beam Algorithm

The pencil beam dose calculation is a widely used dose calculation algorithm in proton radiotherapy providing reasonable accuracy for many situations at fast computation time. Its dose predictions are based on empirical data and analytic calculations. The

modelled pencil beam is divided in sub-beams (19 in RayStation (RS) Version 7) which are individually calculated and then super-positioned to acquire local proton fluence. The dose is a result of the energy loss in a dose voxel and the assigned mass of the voxel. In the most general way, the dose is described by Equation 2.22,

$$D = IDD(z) \cdot \Phi\left(x(z), y(z), z\right) \tag{2.22}$$

where z represents the water equivalent depth, which is determined by the integrated water to medium stopping power ratio, and Φ the lateral dose profile. The lateral distribution is determined by two physical effects, the nuclear scattering and the multiple Coulomb scattering. The complexity of the lateral fluence has a large effect on the quality and speed of the PB calculation. MCS is usually treated analytically, whereas nuclear scattering may be corrected empirically.

Aside from beam and nozzle modelling, which need to be specified for every facility, the input parameter for the dose calculation is the measured IDD in water [40]. Since the dose is calculated to a voxel along the IDD, heterogeneities in the CT voxels can not be accounted correctly leading to deviations in the deposed dose, for example an underdosing in lung tissue. [20]

2.8.1.2. Monte Carlo Calculation

In this model the dose is calculated separately for every voxel by tracking single particles. MC particle transport simulations require usually more computation power and time than PB algorithms but with the steady technological progress this concept becomes more and more favoured. It provides the highest accuracy, especially when tissue heterogeneities need to be considered carefully. The physical interaction of each particle are simulated using a statistical approach by random sampling. In order to achieve statistical accuracy large enough numbers of particles need to be simulated. In a balance between accuracy and computation time a compromise needs to be made to which limits the physical models are applied in terms of range and energy tracking of the primary and secondary particles as well as what types of interactions are relevant for particle therapy.

For particle propagation RS simulates the movement via the "random hinge" method, where two straight lines are connected by a hinge. The angle of the hinge is determined by the MCS. In every traversed voxel the energy loss and the nuclear absorption is calculated, which gives the deposed energy to the voxel. The random hinge is repeated for a particle until its energy falls underneath a threshold (1 MeV), after that the residual range is a straight line. The BP spreading is considered by applying a stopping power correction per each random hinge based on the Bohr approximation (see Equation 2.14). The detailed explanations of concept and implementation are given in the RayStation 7 Reference Manual [40].

3. Materials and Methods

3.1. Measurement Setup for Irradiation

In order to investigate the effect of different materials on the proton pencil beam, profiles were measured in longitudinal (beam direction) and horizontal lateral direction (perpendicular to the beam direction). As can be seen in Figure 3.1 the beam exits the nozzle on the right side and deposes its particles in the water phantom (MP3-PL, PTW-Freiburg, Germany). The investigated materials were positioned in front of the water phantom entrance window on the table (indicated by the black box in Figure 3.1).

Figure 3.1.: Basic setup for measurements

The phantom was made from polymethyl methacrylate (PMMA), commonly known by trade names such as Plexiglas or Lucite, which has properties similar to water. It was filled with 170 L distilled water via a pumping station and a water reservoir installed underneath. The walls were 18 mm wide except for the entrance window for horizontal beams, which was thinner and had a WET of 5.85 mm. On the phantoms entrance window a surface reference detector (3.2.1) was mounted to measure the signal at the beam entrance while a moving detector measured the dose in the depth. The field detector could move along all three axis in a minimal step size of 1 mm and was controlled via a control pendant or via the MEPHYSTO software tool (**Me**dical **Phys**ics **To**ol,

PTW-Freiburg, Germany) installed on a laptop connected to the hardware of the water phantom.

Along the beam (longitudinal) direction IDDs (see Section 2.4) were measured with a large BP field ionisation chamber (3.2.1). Regions along the Bragg curve with a high gradient required a smaller measurement step size. Therefore, the step sizes was set between 0.1 and 4 mm depending on the position along the Bragg curve.

Contrary to IDD profiles a small field detector was required for lateral measurements and therefore a microDiamond (3.2.2) was used. The step sizes of detector movement was set between 1 and 3 mm and covered a range of 5 cm transversal to beam direction. The detector was moving on a horizontal line in transversal direction to the beam and the detector orientation was in axial direction. The depths at which the lateral profiles were acquired were based on previous R_{80} measurements of the different materials to allow comparability.

The first point of interest (POI) inside the water phantom was determined by several factors listed in Table 3.1. The safety margin represents an ideal value which was the limit of the minimal distance between field chamber and the water phantoms inner wall. It needed to be measured and corrected every time the phantom was set up.

Table 3.1.: First possible point of measurement inside the water phantom for the BP chamber, respectively the microDiamond in parenthesis

	[mm]
WET of the MP3-PL entrance window	5.85
WET of the reference detector (Type 34080 SN42)	1.95
Safety margin	0.5
WET of the field detector to the active volume (see 3.2)	4.04 (1)
Total	12.34 (9.3)

As mentioned before, the materials indicated in Figure 3.1, were positioned in the beam path close to the surface of the phantom. All measurements with materials in front of the entrance window were compared to reference measurements in water without an additional material in the beam path (hence referred to as water measurements).

The energies for the experiments were chosen as 97.4 MeV/u and 148.2 MeV/u to be close to clinical applications for lung treatments (based on range in water). These energy values are well documented at MedAustron and are commonly used key energies for any kind of calibration, clinically and for research experiments, respectively.

3.2. Detectors

The charge deposited by the proton beam was collected in the detector, were transferred to the electrometer and from there transmitted to a laptop holding the read-out software MEPHYSTO. Combining the signal measured on the surface of the water phantom (reference signal) with the signal of the moving field chamber gave relative dosimetric results which were then used for evaluation. Each measurement was repeated multiple times to ensure reproducibility.

3.2.1. Bragg Peak Chamber

BP chambers were parallel-plane ionisation chambers (see Section 2.5.1). The reference chamber (Type 34080 SN42, PTW-Freiburg, Germany) was mounted outside on the surface of the water phantom. It had a diameter of 8.16 cm with an active volume of 10.5 cm^3 and a measured WET of 1.95 mm, which was taken into account for precise range measurements. The chamber was connected to an electrometer and operated at 400 V. Pre-irradiation was not required for this detector according to the PTW manual [41].

The field chamber (Type 34070 SN124, PTW-Freiburg, Germany) held the same properties as the reference chamber except that the measured WET from its surface to the active volume was 4.04 mm. It was mounted on the movable arms of the water phantom and collected signals along the central axis of the proton beam to measure IDDs.

3.2.2. Diode Detector

The microDiamond detector (Type 60019 SN122232, PTW-Freiburg, Germany) was a solide state detector with a Schottky diode (see Section 2.5.2). It was used as field detector for lateral profile measurements. Its radius was 1.1 mm with an active volume of 0.004 mm^3 and a WET stated by the producer of 1 mm. The microDiamond detector was operated at 0 V and pre-irradiated with 5 Gy according to the PTW manual [42].

3.3. Lung Substitutes

In general, measuring real lung tissue would provide multiple problems. The main problem was that a deceased organ changes its structure due to internal pressure loss and the lack of fluid and gas circulation. Another problem would the time between irradiation, CT scans and physical measurements. In the meantime natural degradation could not be avoided and due to its consistency positions could not be stabilised. Titt et al. showed in their study [43], that the position of proton beam centre along the lung had large effects on the resulting Bragg curve, which complicated reproducibility of results.

For validation of the ripple filter effect (as explained in Section 2.3.1), lung substitutes were used which bypass the difficulties listed above. The lung substitutes should mimic

the properties of real tissue as good as possible. These included a density of around 0.26 g/cm^3 as well as an atomic material composition of lung tissue [32] and an inhomogeneous structure that is comparable to the alveoli ($0.2 - 0.5$ mm). Detailed properties of the materials are listed in Table A.3 and A.4 in the appendix. The composition information was not used in any calculation, but for evaluation and error estimation of the results.

In order to allow comparability, not only between measurement and simulation of each material, but between measurements of different materials, their physical properties, such as width and thickness, needed to be standardised. This was necessary as the materials were not available in the exact same widths or thicknesses.
The properties of the materials were normalised to 5 cm width and 1 g/cm^2 thickness. The change of the properties of the BP (see Section 3.6.1) by normalisation were investigated with different fit functions. The best fits are shown in the results (4.1.2).

3.3.1. Lung Tissue Equivalent Plates

These plates were manufactured by CIRS (USA) and designed to match the atomic composition of lung. The producer states that these tissue equivalent materials simulate the absorption and scattering properties of real tissue within 1% for electron and photon applications between 0.01 and 100 MeV. These materials were used to create the clinically used scanner specific HU CT calibration curves (see Table A.1).

For measurements, exhale plates with high density and inhale plates with lower density were examined. The plates had a width of 1 cm and were stacked together to 2, 4 and 7 cm for inhale and 2 cm for exhale. This was to increase effects on the beam and evaluate the relation between the BP behaviour and the width of the material penetrated by the proton beam.

During measurements it was found that the densities of single lung inhale plates varied between of -6 % and +10 % of the density 0.195 g/cm^3 as stated by the manufacturer. The effect on the results was smaller as multiple plates were used at once, but was non negligible when comparing the results of different measurement sessions using four 1 cm thick lung inhale Tissue equivalent plates (TEP)s. (samples shown in Figure 3.2a)

3.3.2. Cork

This material was well established as lung substitute and frequently used. Its density and atomic composition was close to lung. During the thesis two different type of corks with different densities had been tested. The higher density sample was taken from a yoga block and was a high compressed cork without any macroscopic visible air cavities. The samples were cut to size by hand to 5.2 and 2.5 cm.

The less dense cork sample was made from multiple thin cork slabs (about 6 mm width

per slab) used for floor noise reduction. The structure of a slab was made from around 1 cm large cork grains glued together and cut in shape. Here macroscopic air cavities were visible. For measurements 4 slabs were taped together in order to have a more pronounced effect on the BP. (samples shown in Figure 3.2b & 3.2c)

3.3.3. Balsawood

The wood is from the tree Ochroma pyramidale, known as balsa. It can be assumed to have an atomic composition which is comparable to real tissue while being lighter than most other woods. It was therefore also in use for lung phantoms, such as ARDOS [44]. With bare eyes the structure of balsawood appeared homogeneous, although it is known that woods have microscopic transport vessels in axial and radial direction. (sample shown in Figure 3.2d)

3.3.4. Floral Foam

The main component of this artificial resin is phenolic resin. The full atomic composition could not easily be obtained, instead, the well known composition of polyurethane was used as a reasonable approximation. In different studies a variety of synthetic foams were tested. Candidates like polystyrene foams tend to be too homogeneous while this foam has an obvious porous structure and had been investigated despite its low density. (sample shown in Figure 3.2e)

3.3.5. Konjac Sponge

This material is made from the root of the plant Amorphophallus konjac, also known as devil's tongue. The root is pulverised and the powder boiled. In the process long polymers are produced which create a foam-like structure. An exact composition could not be found but it was assumed to resemble organic materials and be comparable to tissue. The atomic composition was assumed to be similar to that of a root or a sea sponge. Since the structure of the material changes in the production process, the sponge-like composition seemed better suited than that of a root.

For measurement two konjac sponges were cut to have plane parallel surfaces and taped together to have a material width of about 33 mm. For immobilisation during the measurements the sample was taped to an 1 mm RW3 slab (see Figure 3.2g), which range shifting effect was corrected for the evaluation. (sample shown in Figure 3.2f)

3.3.6. Pumice

The volcanic rock has a heterogeneous structure and a density which matches the one of lung well and was therefore tested despite its abundance of silicon dioxide. The amount of silicon depends on the sample and is varying around 25 %. Since measurements of the atomic compositions are not easy a value from an external source was assumed. The approximation was sufficient here as no exact calculations depending on the composition was performed. (sample shown in Figure 3.2h)

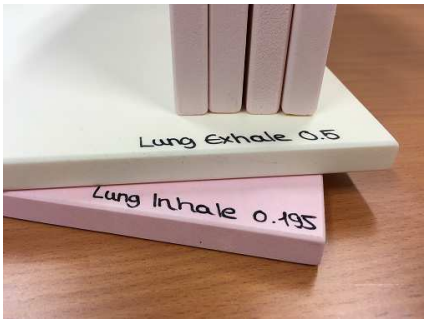

(a) Lung TEPs inhale and exhale

(b) Yoga block cork

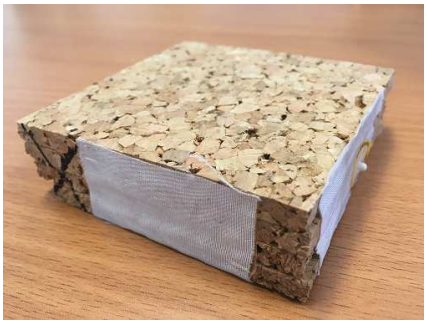

(c) Cork slabs

(d) Balsawood

(e) Floral foam

(f) Konjac sponge

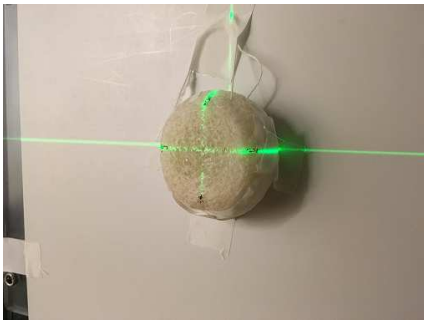

(g) Konjac sponge in measurement setup

(h) Pumice

Figure 3.2.: Different materials which were irradiated and analysed

3.4. Density Determination of Materials

The weight of the sample materials were measured with a scale with an accuracy of 0.01 g. The measurement of the volume was performed different depending on the geometry of the materials.
For the unaltered materials (TEP, cork, floral foam, pumice) basic shapes were used to determine the volume with minor corrections for rounded edges.
For balsawood additional corrections were required as the long sides were not parallel and an additional wedge-shape was added to the box volume.
The konjac sponge could not be described by geometrical shapes and its volume was acquired in two different ways. One was to draw a structure in RayStation which covered the whole visible material. The other was to wrap the sample in a thin plastic foil and measure amount of suppressed water. The volume estimation via RayStation showed deviations also for basic-shape materials due to CT resolution and structure drawing accuracy. Consequently, the latter option was considered better and used for the final konjac volume.

Note that the density calculated this way was defined as bulk density and was written as ρ_{mean} while the true density or approximately skeletal density of the material was written as ρ_{mat}. Latter is multiple times higher than ρ_{mean} for porous materials, because it represents the pure density of the material without any air cavities. A detailed explanation was given by Webb [45]. For example, for lung tissue this would be approximately $\rho_{mean} = 0.26$ g/cm^3 and $\rho_{mat} = 1.05$ g/cm^3
While the determination of the skeletal density might be possible with a gas pycnometer, which was not an option for this study, estimations were taken based on different external sources.

3.5. Hounsfield Units Determination of Materials

Prior to the HU determination of the lung tissue equivalent materials as well as for calculations in the treatment planning system (TPS), CT scans were required. Those were obtained with the CT scanner (PHILIPS Brilliance Big Bore Oncology) at MedAustron and one of the clinically used scanning protocols, which was available and most suitable for lung (Ad_Abdn). The slice thickness was changed from typically 3 mm (clinically used) to 1 mm to increase the resolution in the beam direction (sagittal direction).

The CT images in form of digital imaging and communications in medicine (DICOM) files were evaluated with help of the MICE toolkit (v1.0.9). In order to acquire material specific HUs, 4 box structures with 2 x 2 x 2 cm^3 in size were drawn in MICE within the respective material. As the lung TEP had a width of 1 cm their boxes had the dimention of 2 x 2 x 0.5 cm^3. The 4 boxes were aligned around the central axis where the materials was irradiated during measurements. From the boxes the HU per voxel were extracted, which were around 5700 entries per box, and loaded in a Python (v3.7.2) script for eval-

uation. There the calculated average HU per box was used to determine HU_{mean}. The range of the HUs HU_{range} was determined by calculating the 2σ confidence interval of the HU spectrum. This quantity was used as a parameter to determine the degree of inhomogeneity of the examined materials. The results of the 4 boxes per materials were averaged and the standard deviation calculated.

For the HUs an uncertainty of 2.5 HU was assumed combining the CT scanner uncertainty as described by the quality assurance at MedAustron [46] and the standard deviation of the HU values per box. Instead of a single structure of the whole material, these boxes were chosen to be small enough to investigate the HUs in a region relevant for the proton beam during measurements, but also large enough to give a HU distribution to be representative for the whole material.

3.6. Data Evaluation

3.6.1. Integral Depth Dose Profiles from Measurements

During a measurement session the same material was measured $2-4$ times for reproducibility. The measured BP curves for all materials covered the proximal R_{50} to a distal point, where the detected dose was zero. The data was acquired with the PTW MEPHYSTO software. However, its analyse tool were not used as it interpolates the data points to find the desired POI. This does not take uncertainties of the dose level and position into account. Instead a Python script was created to fit the data points, using least square fit, and thereby obtain the desired range points. In order to find the maximum of the BP a polynomial function of fourth degree was used. For the other POIs a fifth order polynomial was applied. The order of the polynomial was set as low as possible while providing consistent results. The interval of points included in the fit was related to the order of the polynomial. The interval I is given in Equation 3.1.

$$I = \left[-round(\frac{degree}{2}) + 1, ..., \text{POI}, ..., round(\frac{degree}{2}) + 1\right] \tag{3.1}$$

In this equation, POI is the data point closest to the expected POI position. The step size within the interval was set to 1 µm. This approach was chosen because it could be applied to all measurements in the same way. The measurement steps size needed to be adjusted manually during measurement and therefore the density of data points around individual POIs was different.

The POIs, which were investigated in more detail, were the maximum (necessary to determine the ranges at certain percentage of the BP height precisely), the distal R_{80} for WET calculations and the proximal and distal R_{50} as characteristic quantity for the BP spreading.

Water Equivalent Thickness

The WET was defined as the range difference between the R_{80} of water and the sample (see Equation 3.2).

$$WET = R_{80,wat} - R_{80,mat} \tag{3.2}$$

In Figure 3.3 an example is shown to display the acquisition of the R_{80}. It was found

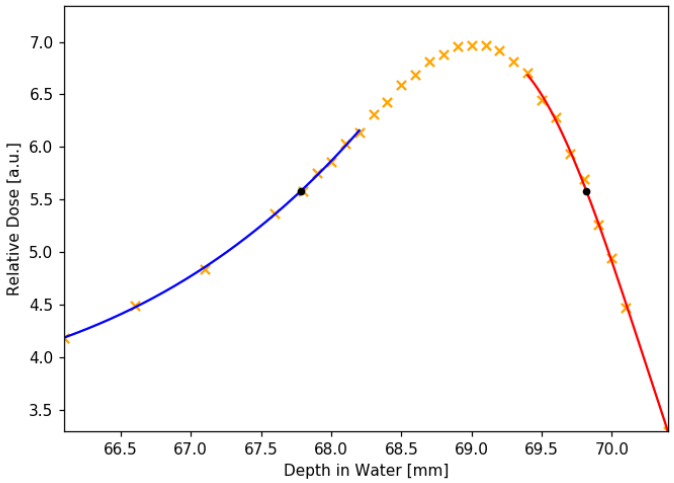

Figure 3.3.: Proximal and distal R_{80} in water at 97.4 MeV from the IDD measurement

by Andy Koehler that the R_{80} is almost invariant when the shape of the BP changes [34].

On a closer look a slight wobbling of the data points was visible. Two data points were measured per synchrotron spill and a correlation to either the beam or the detector movement was thus possible. This uncertainty justified the fit functions over an interpolation. The absolute ranges were not investigated but only the range offsets caused by the materials. The error was calculated from the propagation of the standard deviation (STD) of R_{80} (see Equation 3.3).

$$\delta WET_{error} = \sqrt{\delta {R_{80}}^2_{STD,wat} + \delta {R_{80}}^2_{STD,mat}} \tag{3.3}$$

Bragg Peak Spreading

Additionally to the range shifting effect of materials, the caused BP spreading was investigated. As it is well known [30, 31, 43, 47, 48, 49] not only the composition of a material contributes to the BP spreading but also the geometrical distribution of matter. In order to classify the spreading of the BP the quantity σ was used which was derived

from the full width half maximum (FWHM).

$$\sigma_{measurement} = \frac{\text{FWHM}}{2\sqrt{2\ln(2)}} = \frac{R_{50,distal} - R_{50,proximal}}{2\sqrt{2\ln(2)}} \tag{3.4}$$

While a Bragg Peak is clearly not a Gaussian and σ can normally not easily be calculated this way, it was assumed that the contribution of the material to the BP spreading was a normal distribution, as given by the Bohr approximation (see Equation 2.14. This assumption seems to be justifiable, if only the material part of BP width was treated as the standard deviation of a Gaussian.

$$\sigma_{mat}^2 = \sigma_{measurement}^2 - \sigma_{wat}^2 \tag{3.5}$$

For sake of simplicity σ_m[1] was derived according to Equation 3.4 and 3.5, while for example Ringbæk et. al. [47] determined σ_m by convoluting a Gaussian (see Equation 3.7) with the pristine BP and fitted the parameter of the Gaussian function.

Due to the BP spreading the peak height decreased and the position of the proximal R_{50} was more in the flat region of the Bragg curve. To test if the changed position of the R_{50} had an additional effect on σ_m the ratio of the R_{80}-width to the R_{50}-width were compared between water and cork (lowest maximum). It was found that the relative ratio only changed by 1.5 %, therefore the derived σ_m was found to be a valid BP quantity and suitable for further investigations.

For an estimation of the uncertainty of the results the STD of the FWHM of the measurements was derived. An error propagation from the FWHM of the measurement to the σ_m of the material was applied under the assumption of random and uncorrelated errors. Contrary to WET, σ_m and its error were calculated from all available measurements since the BP spreading was unaffected by range offsets.

3.6.2. Lateral Profiles from Measurements

For lateral profile evaluation again a Python script was used. The investigated POI was the maximum and the position at 50 % and 10 % of the profiles maximum. Each POI was determined by fitting a polynomial of degree 4 with an interval size according to Equation 3.1. From the POIs at 10 % and 50 % height the width of the curve was calculated and extracted. The averaged values and the STDs of the repeated measurements were used for evaluation.
The measured profiles were obtained at various depths. Those depths were chosen as 50, 80, 90 and 97.5 % of the R_{80} of the material, which was obtained from IDD measurements.

[1] from now on σ_{mat} is written as σ_m

3.6.3. Simulations of the Treatment Planning System

3.6.3.1. Integral Depth Dose Profiles

In RayStation 7 simulations with the Monte Carlo dose engine 4.1 and a calculation uncertainty of 0.5 % were performed. The setup of the experiments was reproduced as close as possible with a beam traversing the material in sagittal direction of the CT image. To simulate an IDD multiple beam spots was used in a 2 x 2 cm^2 field in order to simulate the detector geometry. Parallel to the point where the beams passed through the material another set of beam was created. This one did not go through the material but only through water. Otherwise it had the same settings and was used as a water reference in the corresponding CT image.

The CT scans of the materials had a resolution[2] of 1.17 x 1.17 mm^2 in the axial plane and 1 mm in sagittal (longitudinal to the beam) direction. Dose grid voxels were aligned to the CT voxels. However, the smallest dose grid step size was in 0.1 mm steps. Therefore, the grid size was set to 1.2 x 1.2 x 1 mm^2 and the alignment of the dose grid to the CT grid was done closest possible to the beam centre. RayStation calculated the dose at the centre of each voxel and the dose values were linearly interpolated in 0.1 mm steps to the next voxel centre.

The beam profiles were acquired using the "Line Dose" tool in RayStation, which gives the dose at a certain position in 0.1 mm steps. The created csv-files were loaded into Python and evaluated there. Dose interpolation was deactivated in RayStation. By doing that the dose value was constant within a voxel. As RS calculates the dose of a voxel at its centre only the central value was kept for evaluation. Since the resolution (1 data point per mm) is not high enough to apply the fit functions used for measurements, the functions needed to be adapted for the maximum and the distal region of the BP. In the proximal region a polynomial of degree 5 was used. By comparing the results of the fits to the higher spacial resolution measurement data for the maximum a second order polynomial fit was most accurate. Due to the lack of available data points in the distal fall off region a Gaussian fit was used as an approximation such as described by Bortfeld [50]. The Gaussian fit showed good agreement within the R_{80} and the R_{20}, but started deviated outside this distal fall-off region.

3.6.3.2. Lateral Profiles

The setup in the TPS was the same as for the IDDs but instead of a field of beam spots only a single spot (sinlge pencil beam) was used. As no effect on the lateral beam spreading was to be expected, only profiles, obtained in RS, for the 5.2 cm cork and the water reference were evaluated. The cork was chosen because from the results of the IDD measurements, it was concluded that any effect would be most likely visible for the cork sample, since it affected the proton beam the most. The same POIs were

[2] in clinical settings the standard resolution is $\frac{\text{field of view [mm]}}{\text{matrix elements per direction}} = \frac{600}{512}$

determined as for the lateral profile measurements and were acquired by the same fit functions. A precise evaluation of the lateral profiles in RS at a certain depth was not possible. This was due to uncertainties in the exact determination of the R_{80} as well as the 1 mm dose grid resolution in beam direction. Instead the lateral profiles were obtained at the position with the highest dose value, which therefore was closest to the BP maximum and compared to the measurements at 97.5 % of the R_{80}.

3.7. Analytical Model for the Bragg Peak Spreading

Based on the work of Titt et. al. [43] an analytical calculation model was tested to determine the BP spreading caused by inhomogeneous materials. By assuming the irradiated inhomogeneous obstacle could be described as a voxel model an interaction probability could be modelled as a binomial distribution (Equation 3.6). Where k is the number of non empty voxels in a line of voxels n (representing the materials width W) through the material with a probability p of encountering a filled voxel.

$$P(k) = \binom{n}{k} p^k (1-p)^{n-k} \tag{3.6}$$

For large numbers of n Equation 3.6 converges to a normal distribution,

$$f(x;\mu,\sigma) = \frac{1}{\sqrt{2\pi\sigma^2}} e^{-\frac{(x-\mu)^2}{2\sigma^2}} \tag{3.7}$$

were σ becomes

$$\sigma^2 = n(p-p^2). \tag{3.8}$$

Instead of a width of the voxel field n, Titt et. al. [43] described the radiological depth (discrete form in Equation 3.9) as a function of the geometrical depth x. Where d is the size of the voxel and S_i is the stopping power ratio of a voxel, so either 1, if filled, or 0 in air or vacuum.

$$\zeta(x) = d \sum_{i=1}^{n} S_i \tag{3.9}$$

The variance of radiological depth is then given as

$$\sigma^2(x) = d^2 \sum_{i=1}^{n=\frac{W}{d}} (\langle S_i^2 \rangle - \langle S_i \rangle^2). \tag{3.10}$$

With the expectation values of $\langle S_i \rangle$ and $\langle S_i^2 \rangle$ are p, or p^2 respectively, Equation 3.10 then becomes

$$\sigma^2 = d \cdot W(p-p^2). \tag{3.11}$$

Since the probability of encountering a filled voxel depends on the pore size the equation is hard to solve for materials not representable in a voxel model. In this thesis, Equation 3.11 was modified to be applicable for the HU information derived from the

CT scans. Here, the voxel size d of a material represents the voxel size of a CT image. The probability p represents the filling state of the material, see Equation 3.12. It was assumed that p could be rewritten to represent the ratio of the density of the material with contribution of pores (ρ_{mean}) and without (ρ_{mat}).

$$p = \frac{V_{filled}}{V_{tot}} = \frac{\frac{V_{filled}}{m}}{\frac{V_{tot}}{m}} = \frac{\rho_{mean}}{\rho_{mat}} \tag{3.12}$$

In a further step the density was replaced with the Hounsfield values of HU-density calibration table and shifted by 1024 to start the scale at 0.

$$\sigma^2 = d \cdot W \cdot \left(\frac{HU_{mean}}{HU_{mat}} - \left(\frac{HU_{mean}}{HU_{mat}} \right)^2 \right) = d^2 \cdot n \cdot \frac{HU_{mean}}{HU_{mat}} \left(1 - \frac{HU_{mean}}{HU_{mat}} \right) \tag{3.13}$$

HU_{mean} is the value of the average HUs in the material and HU_{mat} represents the theoretical HU if the material would not contain pores. Finally, Equation 3.13 has been rewritten to

$$\sigma^2 = d^2 \cdot \sum_{i=1}^{n} \left(\frac{HU_i}{HU_{mat}} \right) \left(1 - \frac{HU_{mean}}{HU_{mat}} \right), \tag{3.14}$$

where HU_i are the HU values of the CT voxels along the central beam axis in the planning CT and considered the HU variation in the material. The heterogeneity induced BP spreading is a consequence of particles experiencing different densities along their path as shown in Figure 2.3. In Equation 3.14 HU only the variation longitudinal to the beam was considered. However, the density distribution was assumed to be isotropic for large numbers of traversed voxels n.

Equation 3.14 assumes a Gaussian contribution of the inhomogeneous geometrical effects to the longitudinal spread of the BP. For for pure homogeneous materials ($p = 1$) σ is zero. This effect σ_{inho} should then be an additional effect to the 'natural' contribution of the BP width in water σ_{wat} and the homogeneous material contribution σ_{hom}.

$$\sigma_{tot}^2 = \sigma_{wat}^2 + \sigma_{hom}^2 + \sigma_{inho}^2 \tag{3.15}$$

3.8. Modulation Power

In the work of Witt [48] and subsequent works of others [47, 49, 51] a material specific parameter was derived, called modulation power (MP). It was meant to be an analogy to the stopping power and scatter power (see Section 2.2). It was used to describe the Bragg peak spreading relative to the range shifting of a material and gave information about the geometrical effect on the BP spreading. This information was independent of the thickness of the material [47].
The modulation power was defined as

$$P_{mod} = \frac{\sigma^2}{\mu} \tag{3.16}$$

based on the assumption a Gaussian-like effect (see Equation 3.7) of the material on the BP. There, σ represented the material-induced spreading of the BP and μ the range shift relative to the reference BP in water. Therefore, σ was associated with σ_m and μ with the WET. It was given in units of g/cm^2 or mm, depending on the definition of σ and WET.

By definition of the developer of the modulation power concept, it was supposed to be a modification factor from homogenous to heterogeneous materials, therefore σ^2 in Equation 3.16 should actually be σ^2_{inho}. Throughout this thesis both versions of P_{mod} will be given as $P_{mod,m}$, when σ_m was used, and $P_{mod,inho}$, when σ_{inho} was used.

4. Results

4.1. Integral Depth Dose Measurements

4.1.1. Preparation of Data

All data was collected in three measurement sessions, $6 - 8$ hours each. The individual measurements were listed in Table A.2 in the appendix. During the data evaluation, a dependency of the moving direction of the detector to the BP position between 0.05 and 0.13 mm was found, as a consequence only one direction per measurement session was used in the data analysis.

Another offset was observed as a range variation between water measurements of different measurement sessions. This was most likely due to measurement uncertainties of the

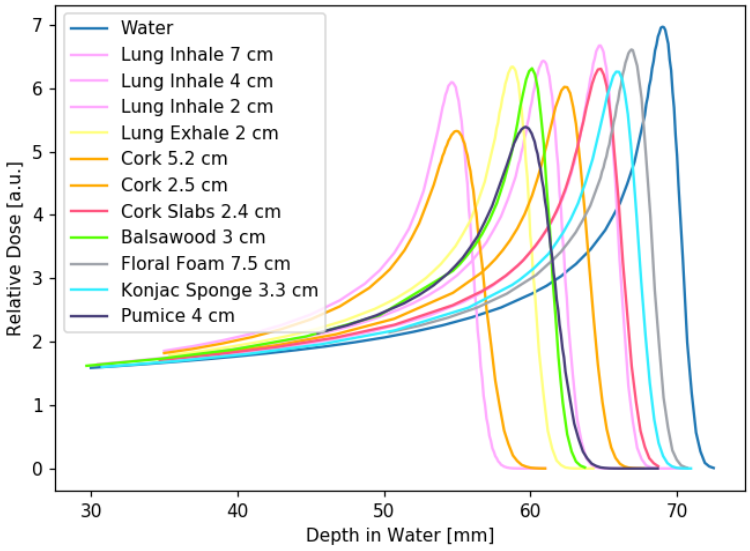

Figure 4.1.: IDD profiles at 97.4 MeV

safety margin for determining the detectors first point of measurement (see Table 3.1). In order to achieve comparability of results, all measurements of one measurement session were shifted by the relative range offset of the water reference measurements. During the proton commissioning at MedAustron a specific range was defined for 97.4 MeV and

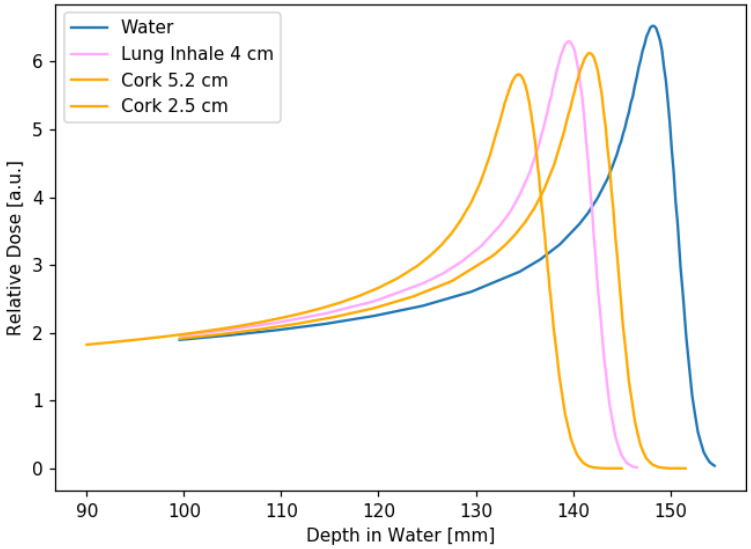

Figure 4.2.: IDD profiles at 148.2 MeV

148.2MeV. The water ranges from the second measurement session were closest to the commissioning ranges and therefore the ranges of the other two measurement sessions were shifted to match the ranges of the second one.

Figure 4.1 and 4.2 show one IDD of each measured material at 97.4 MeV and 148.2 MeV. The IDD properties, which were investigated most, were the quantities for the range shifting (WET) and the BP spreading (σ_m). The derived results are listed in Table 4.1 together with the normalised WET and σ_m.

4.1.2. Fitting and Normalisation of IDD Properties

In order to evaluate how the WET and σ_m changed for different widths of the same material, the lung inhale TEPs and additionally the two pieces of cork from the yoga block were used to test different fit functions. The latter were used to see if the fit function holds for inhomogeneous materials. On basis of the fit functions, which agreed best the properties of the materials, were normalised to the same width and thickness.

In Figure 4.3a and 4.3b the applied fit functions were a linear fit (in blue) and a square root fit (in red) in the least square approximation. A constant fit parameter p_0 was included to allow for uncertainties in the water measurement as WET and σ_m were relative quantities[1]. The error bars in Figure 4.3 represented the STD of the WET and σ_m

[1] p_0 was found to be smaller than $\sigma_{STD,wat}$

on the y-axis and the uncertainty of the width were obtained by repeated measurements and small position variations on the x-axis.

$$f(W) = p_0 + p_1 \cdot W \text{ and } f(W) = p_0 + p_1 \cdot \sqrt{W} \tag{4.1}$$

The best results were found as a linear fit for the WET as a function of width and thickness of the material. For σ_m the square root fit agreed best.

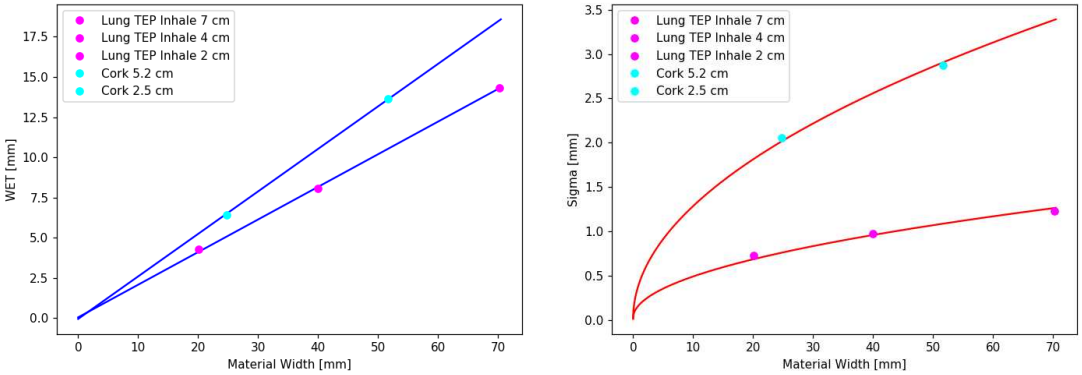

(a) Linear fit for $WET(D)$ (b) Square root fit for $\sigma(D)$

Figure 4.3.: Linear (blue) and square root (red) fit for different material properties

As shown in Figure 4.3 the applied fits worked for homogeneous and inhomogeneous materials. The verified correlations were used to extract functions for all other samples. The materials were then normalised to 5 cm width and 1 g/cm^2 thickness and the different normalisations were summarised in Figure 4.4 with a representative of each material. The normalised values shown in Table 4.1 with their corresponding STDs rescaled for the normalised WET and σ. Further a 0.1 mm measurement uncertainty of the width of the materials was considered in the error propagation.

The IDD properties normalised to the width of the material were useful for statements about the observable effects in measurements as the width could vary easily in contrast to the density. On the other side, the properties of normalised thickness could be used for statements with respect to the physical properties of a material, such as stopping power or structure. In the following section (4.1.3) different sample properties were plotted against each other and discussed.

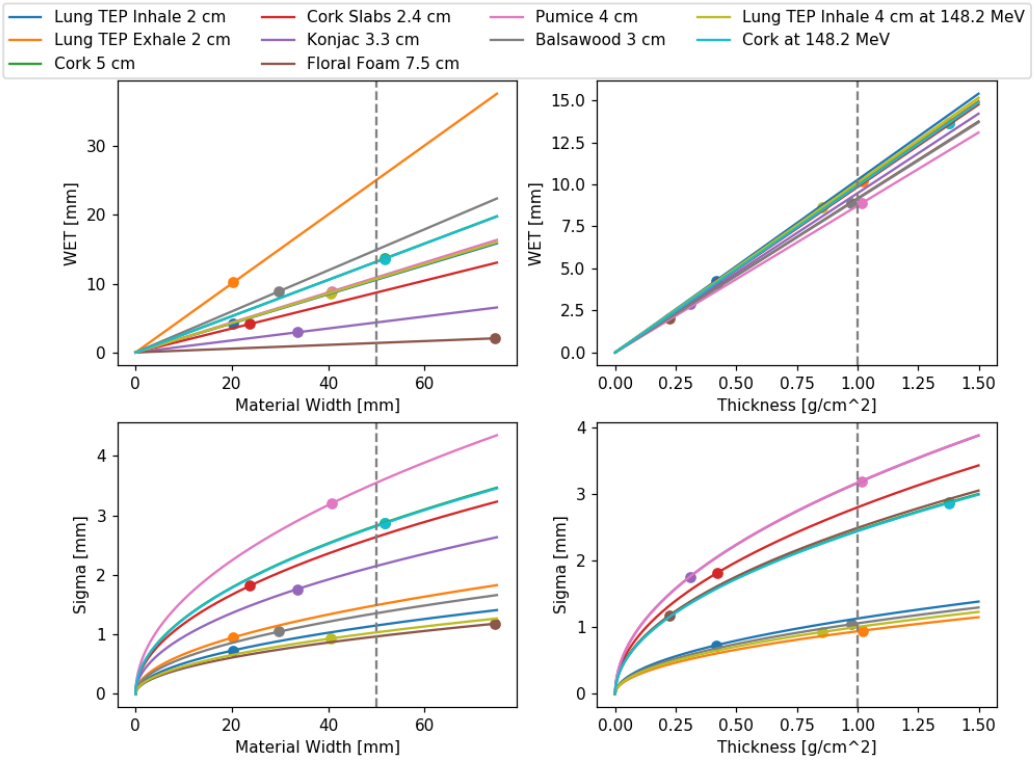

Figure 4.4.: Normalisation function for σ_m and WET of material width and thickness for different materials and energies

Table 4.1.: WET and σ_m as derived from the IDD measurements and normalised to 5 cm and 1 g/cm^2

	Measurements		Width: 5 cm		Thickness: 1 g/cm^2	
[mm]	WET	σ_m	WET	σ_m	WET	σ_m
			97.4 MeV			
Lung TEP Inhale 2 cm	4.26 ± 0.00	0.73 ± 0.00	10.58 ± 0.05	1.15 ± 0.01	10.27 ± 0.05	1.13 ± 0.00
Lung TEP Inhale 4 cm	8.06 ± 0.01	0.98 ± 0.01	10.09 ± 0.03	1.09 ± 0.01	10.17 ± 0.03	1.10 ± 0.01
Lung TEP Inhale 7 cm	14.30 ± 0.03	1.23 ± 0.00	10.18 ± 0.03	1.04 ± 0.00	10.15 ± 0.03	1.03 ± 0.01
Lung TEP Exhale 2 cm	10.19 ± 0.00	0.95 ± 0.01	25.09 ± 0.12	1.49 ± 0.02	9.99 ± 0.05	0.94 ± 0.01
Cork 5.2 cm	13.65 ± 0.01	2.88 ± 0.01	13.21 ± 0.03	2.83 ± 0.01	9.93 ± 0.02	2.45 ± 0.01
Cork 2.5 cm	6.42 ± 0.01	2.06 ± 0.00	12.94 ± 0.05	2.92 ± 0.01	9.73 ± 0.04	2.54 ± 0.01
Cork Slabs 2.4 cm	4.13 ± 0.02	1.82 ± 0.01	8.71 ± 0.05	2.64 ± 0.02	9.84 ± 0.06	2.80 ± 0.03
Balsawood	8.90 ± 0.01	1.05 ± 0.01	14.93 ± 0.05	1.36 ± 0.02	9.13 ± 0.03	1.06 ± 0.01
Floral Foam	2.05 ± 0.01	1.18 ± 0.00	1.38 ± 0.01	0.97 ± 0.00	9.17 ± 0.04	2.49 ± 0.01
Konjac Sponge	2.92 ± 0.01	1.76 ± 0.00	4.36 ± 0.02	2.15 ± 0.01	9.48 ± 0.05	3.17 ± 0.02
Pumice	8.86 ± 0.01	3.20 ± 0.00	10.91 ± 0.03	3.55 ± 0.01	8.73 ± 0.02	3.17 ± 0.01
			148.2 MeV			
Lung TEP Inhale 4 cm	8.65 ± 0.01	0.93 ± 0.01	10.69 ± 0.03	1.04 ± 0.02	10.11 ± 0.03	1.01 ± 0.02
Cork 5.2 cm	13.63 ± 0.00	2.87 ± 0.00	13.18 ± 0.03	2.82 ± 0.00	9.91 ± 0.02	2.44 ± 0.00
Cork 2.5 cm	6.43 ± 0.01	2.08 ± 0.01	12.96 ± 0.05	2.96 ± 0.02	9.75 ± 0.04	2.57 ± 0.02

4.1.3. Material Characterisation

4.1.3.1. Normalised Thickness

The relation between WET and thickness was plotted in more detail in Figure 4.5, where the WET normalisation to 1 g/cm^2 material thickness was applied and the results were shown with scaled errors. The WET of most materials was within ±5 % of the averaged WET (9.79 mm) of all materials (pumice excluded). The deviation was more than 6 % for the floral foam and the balsawood and over 10 % for the pumice. The WET was primary determined by the width and the density of the material if the composition was roughly the same (see Equation 2.17).

From the differences between the lung TEP inhale and the 5.2 cm and 2.5 cm thick cork it was concluded that, the differences of the WET for most of the materials was most likely due to uncertainties in the precise determination of the local thickness at the proton beam centre rather than the impact of the atomic composition on the stopping power. The materials which had a noticeable different WET, as shown in Table 4.1,

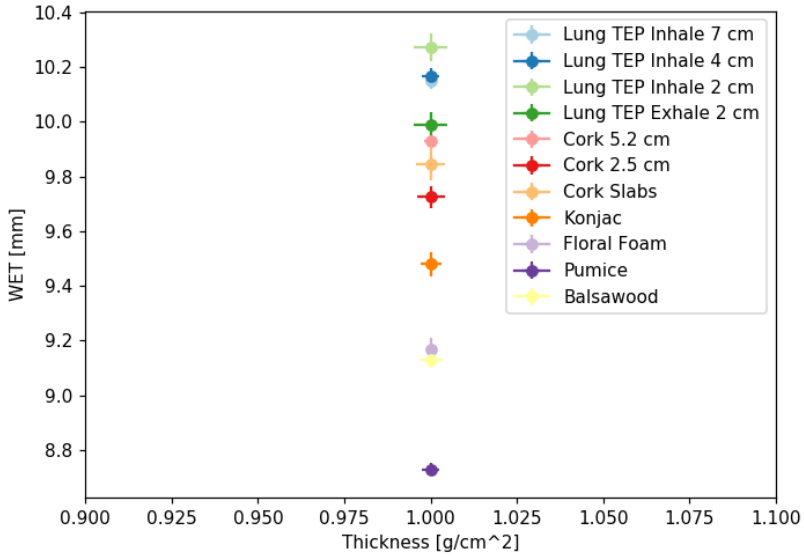

Figure 4.5.: Thickness - WET for material thickness normalised to 1 g/cm^2

were the balsawood, the floral foam and the pumice. For latter this was most likely due to a significant different stopping power caused by the amount of silicon in the material (see the composition in the Appendix, Table A.3).

In the plot of σ_m-thickness in Figure 4.4 two groups of materials were found. This grouping was shown in Figure 4.6 in more detail, but instead of thickness the WET was used on the x-axis. By normalisation of the thickness the effects of the density and the

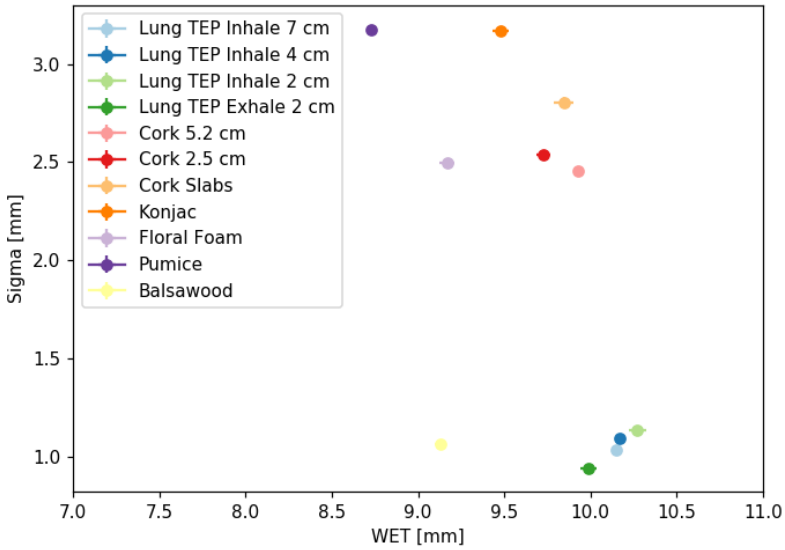

Figure 4.6.: WET - σ_m for material thickness normalised to 1 g/cm^2

width were no longer relevant as parameters for σ_m, which showed the largest effect for the low dense floral foam.

For the normalised thickness, σ_m was mostly influenced by the composition and the inhomogeneities. As the materials had similar atomic compositions the largest contribution to the spreading of the Bragg peak were the density heterogeneities. Consequently, the lung TEPs and the balsawood could be classified as homogeneous materials while the cork, the konjac sponge, the floral foam and the pumice were inhomogeneous. This inhomogeneity effect was relevant and important for a good lung substitute as the avioli contribute essentially to the structure of real lung tissue. [43].

4.1.3.2. Normalised Width

Comparing materials with normalised width allowed more practical conclusions. While the normalised thickness showed a large σ_m for the floral foam, σ_m was small for the normalised width. Its low density suppressed the Bragg peak spreading effect caused by the inhomogeneous structure and therefore made the effect irrelevant under practical conditions. In Figure 4.7 it could be seen that the materials classified as homogeneous, namely balsawood and the lung TEP, showed a smaller σ_m, while the heterogeneous materials (except floral foam) had a larger σ_m (see Table 4.1).

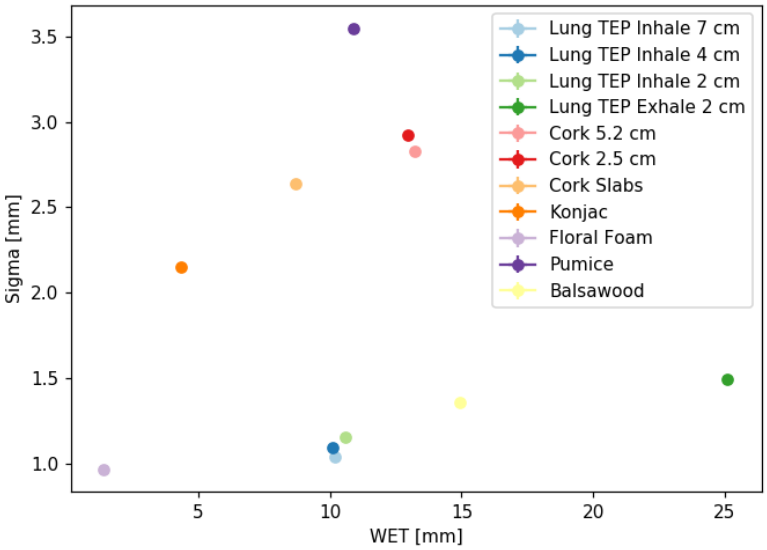

Figure 4.7.: WET - σ_m for material width normalised to 5 cm

4.1.3.3. Energy Dependence

In the previous section 4.1.3 only the measurements with 97.4 MeV were evaluated in more detail. The effect of the proton energy on the Bragg peak spreading will be discussed in the following. In Figure 4.8 the WET and σ_m were plotted against each other for the samples that were measured. WET and σ_m for the respective material were comparable for both energies.

In Table 4.1 it could be seen, that the difference of WET between 97.4 and 148.2 MeV for the 2.5 cm thick cork was 0.01 mm and 0.02 mm for the 5.2 cm thick cork. For the lung plates the difference was about 0.59 mm. This was most likely due to setup uncertainties as not the exact same lung inhale TEPs was used at 97.4 and 148.2 MeV and those had slightly different densities as mentioned in Section 3.3.1. However, similar plates to the ones used for measurements at 148.2 MeV were used for the lung TEP inhale 2 cm measurements. The WET normalised to 5 cm in Table 4.1 for the 2 cm thick inhale plates at 97.4 MeV and for the 4 cm inhale plates at 148.2 MeV differed only by 0.11 mm. This showed that the difference of the WET for the lung TEPs in Figure 4.8 was material related and not energy related.

For σ_m the largest difference between 97.4 and 148.2 MeV were found to be 0.04 mm for the 4 cm thick lung inhale plates, which was equivalent to less than 5 % relative deviation between them. For σ_m of the 2.5 and 5.2 cm thick cork samples the relative deviation between 97.4 and 148.2 MeV was about 1 % each.
From the relativistic Bohr approximation of the BP spreading in Equation 2.14 an energy

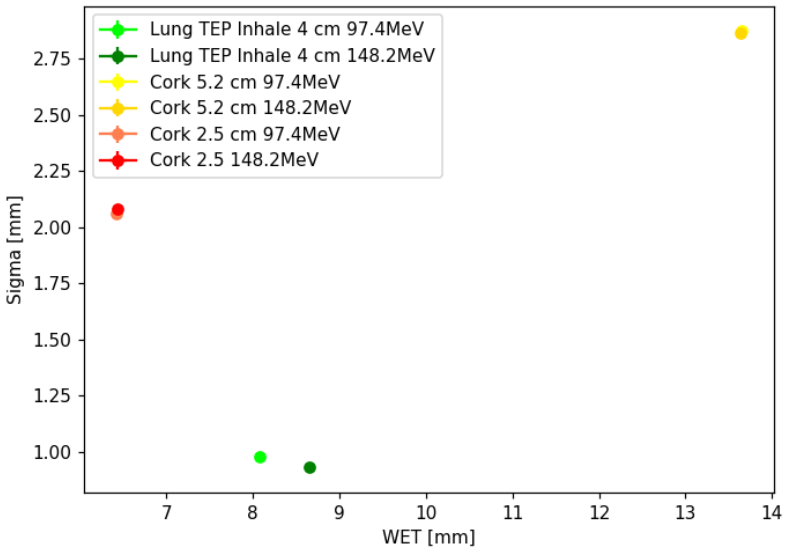

Figure 4.8.: WET - σ_m for materials at 97.4 MeV and 148.2 MeV

dependence via β was assumed. 97.4 MeV proton energy corresponds to about 42 % of speed of light and 148.2 MeV to about 50 %. Therefore, according to the Equation 2.14, σ_m should increase by about 4 % at the higher energy. However, no such increase was observed. Probably due to uncertainties in the setup σ_m was found to be even smaller at 148.2 MeV than at 97.4 MeV for the 5.2 cm thick cork and the 4 cm lung inhale plates.

The results showed no energy dependence for WET or σ_m at treatment relevant energies.

4.1.4. Inhomogeneity Effect

4.1.4.1. Inhomogeneous Contribution to Bragg Peak Spreading

The plot presented earlier in Figure 4.7 showed two groups of materials. One group comprised the homogeneous materials (balsawood, lung TEPs inhale and exhale) and the other the inhomogeneous materials (konjac sponge, cork, floral foam and pumice). The WET was similar to the thickness, but additionally contained information concerning the stopping power and was less prone to uncertainties in the width and density determination, therefore the relation for σ_m to WET was given as

$$\sigma_m^2 \propto \text{WET}. \tag{4.2}$$

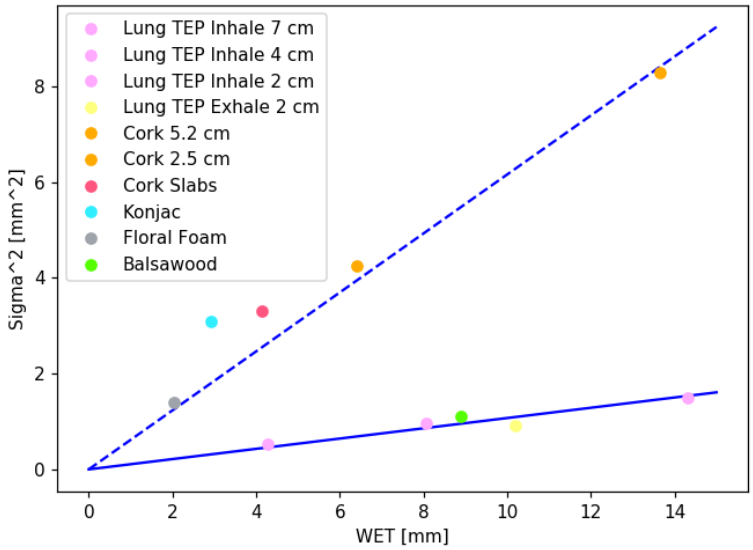

Figure 4.9.: WET - σ_m^2 with linear fit for all homogeneous materials and the two yoga cork samples

Here, the question arose if it was possible to extract the inhomogeneous contribution by deducting the homogeneous part as following:

$$\sigma_{inho}^2 = \sigma_m^2 - \sigma_{hom}^2 \tag{4.3}$$

A fit function was used for all homogeneous materials and, for comparison, another to describe the two yoga cork samples. The latter fit function was used to examine if the heterogeneity of the cork had an effect on the WET - σ_m relation, as tested for the width in Section 4.1.2. In Figure 4.9 the linear fit for the homogeneous materials was depicted with a solid line and with a dashed line for the corks. Note that the gradient of the linear function was basically the modulation power as described in Section 3.8.

For the homogeneous fit the largest deviation between measurement point and fit point was for the exhale TEP with 0.19 mm^2 (-17 %). The deviation was 0.13 mm^2 (-1.6 %) for the 5.2 cm thick cork and 0.29 mm^2 (7 %) for the 2.5 mm thick cork.

First, it was assumed that the homogeneous materials have only a homogeneous contribution σ_{hom} to the BP spreading, which was determined by the composition and the thickness and not the geometry ($\sigma_{inho} = 0$). Second, it was assumed that the homogeneous contribution σ_{hom} was similar for the investigated materials. As the gradient of the linear fit curve in Figure 4.9 was also determined by the inhomogeneity it was concluded that the cork slabs and the konjac sponge have a higher degree of inhomogeneity than the two samples of the yoga cork and the flower sponge.

Table 4.2.: Inhomogeneous and homogeneous contribution to the Bragg peak spreading

	σ_{inho}	σ_{hom}
Cork 5.2 cm	2.61	1.21
Cork 2.5 cm	1.88	0.82
Cork Slabs 2.4 cm	1.69	0.67
Floral Foam	1.08	0.47
Konjac Sponge	1.67	0.56

The linear function found for fitting the homogenous materials was then used to subtract the homogeneous contribution, according to Equation 4.3, from the σ_m^2 of the heterogeneous samples. The derived inhomogeneous contribution to the BP spreading was shown in Table 4.2. It could be seen that the heterogeneous contribution σ_{inho} to the BP spreading was $2-3$ times larger than the homogeneous contribution σ_{hom}. Further, the homogeneous contribution σ_{hom} was given as

$$\frac{\sigma_{hom}^2}{\text{WET}} = 0.10723 \text{ [mm]}, \tag{4.4}$$

which needed to be considered when one aims to calculate the BP spreading via the voxel model described in Section 3.7 as σ was supposed to vanish for homogeneous materials in Equation 3.11.

4.1.4.2. Relation Between Hounsfield Units and Bragg Peak Spreading

Another aspect of this thesis was to investigate if the spreading of the BP could be related to the Hounsfield units, however, not the average HU in the material, but the range of HU. The WET, normalised to the same material width, was linearly related to the average HUs. This was due to linear relations between the density and the WET as well as to the average HU for materials with similar composition and same width (relevant figures were included in the appendix (Figures A.1 to A.3)).

The range of HUs was defined as the width of a spectrum of Hounsfield units. The HU where obtained from a volume representative for each material as described in Section 3.5. The HU spectra are shown in Figure 4.10 as the sum of all 4 boxes per material. The envelopes in this figure were kernel density estimations and were solely used for visualisation. For comparison of the HU spectrum of the materials to real lung tissue, the HU spectra of 4 different lung CT images were added in the appendix (Figure A.4). In Figure 4.10, the konjac sponge and the balsawood showed a visible asymmetry in the distribution of HU. This was interpreted as a consequence of local regions with different HU distributions, which became apparent by plotting the individual HU box histograms for the balsawood. Consequently, it was found that the average and the range of Hounsfield

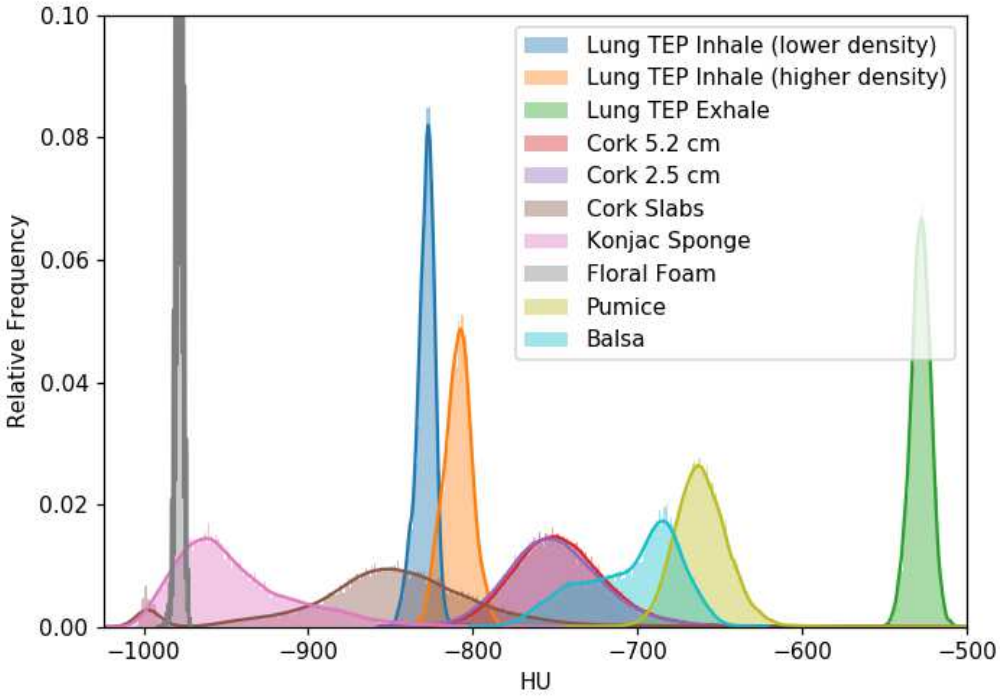

Figure 4.10.: Spectra of Hounsfield units for different materials

units were not independent of the position and the size of the investigated CT image volume. Also the spectrum of the cork slabs had another peak close to minus thousand HU, which were macroscopic air cavities within the material and were neglected in the determination of HU_{mean} and HU_{range} (a threshold was set at -970).

The calculated HU_{mean} and HU_{range} for the lung substitutes as well as for real lung tissue are shown in Table 4.3. The HU_{range} values were compared to different parameters of the IDD derived earlier, especially the BP spreading. As the HU_{range} was independent of the material width as well as of the density, a comparison to the σ_m of the normalised thickness seemed most reasonable. In order to find a correlation between the HU_{range} and the σ_m different fit functions had been tested. The aim was to find a very simple and fast prediction of the BP spreading based on the HU_{range}. On the assumption that σ_m vanished for $HU_{range} = 0$ and that the floral foam and the pumice were not reasonable represented by the HU spectrum and excluded in the fitting, the best results were found for a square root fit shown in Figure 4.11.

The deviation between fit and σ_m was largest for the balsawood with 1.05 mm (-50 %). As mentioned earlier, the size of the box affected the HU distribution for balsawood and lead to an overestimation of the HU_{range}, as it scaled more with the box size than other

Table 4.3.: Average and range of Hounsfield units for different materials

	HU_{mean}	HU_{range}
Real Lung	-828 ± 42	282 ± 56
CIRS Lung Exhale TEP	-528 ± 3	25 ± 1
CIRS Lung Inhale TEP (higher density)	-809 ± 4	32 ± 3
CIRS Lung Inhale TEP (lower density)	-828 ± 4	22 ± 1
Cork 5.2 cm	-746 ± 4	117 ± 2
Cork 2.5 cm	-749 ± 4	122 ± 5
Cork Slabs	-844 ± 5	196 ± 19
Balsawood	-704 ± 7	102 ± 3
Floral Foam	-978 ± 3	8 ± 0
Konjac Sponge	-944 ± 6	138 ± 4
Pumice	-660 ± 5	63 ± 5

materials. The relative deviation between the fit function and σ_m for the konjac sponge was about 29 % and less than 10 % for the different TEP and cork samples.
The ratio between σ_m and HU_{range} is given in Equation 4.5

$$\frac{\sigma_m^2}{HU_{\text{range}}} = 0.0437603 \cdot W \cdot \rho_{mean} \tag{4.5}$$

where the product of material width W times density ρ_{mean} was one and HU_{range} was obtained as the 2σ confidence interval.

Since the HU spectrum depended on the box size and position it could be concluded that HU_{range} was not sufficient to describe the BP spreading precisely and merely a rough correlation could be established via Equation 4.5. Further investigations of the HU distribution in balsawood (not shown here) revealed that the local inhomogeneity and the gradient of the variation of HU had also notable effects on the BP spreading. Also by comparing the HU spectra of real lung tissue to the spectra of materials, it was seen that the idea of a confidence interval could not be easily applied to represent the HU_{range} of living tissue. Those did not have a delimited distribution like the lung substitutes, but had a HU distribution between -1000 and up to 300 HU.

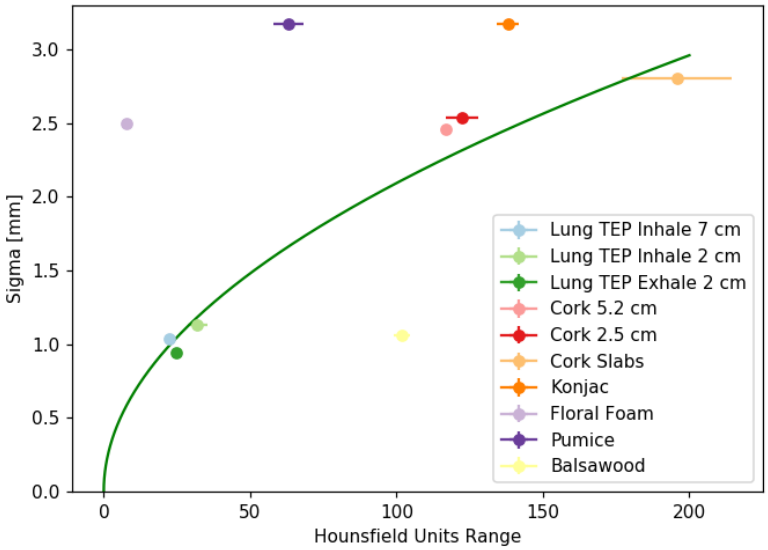

Figure 4.11.: HU range - σ_m for materials tickness normalised to 1 g/cm^2 with square root fit function

4.1.4.3. Modulation Power

As explained in Section 3.8 the modulation power was defined to describe the inhomogeneity effect of material. The calculated modulation per material was given in Table 4.4, where

$$P_{mod,m} = \frac{\sigma_m^2}{\mathrm{WET}} \tag{4.6}$$

was the modulation power derived from the σ_m of the materials and

$$P_{mod,inho} = \frac{\sigma_{inho}^2}{\mathrm{WET}}. \tag{4.7}$$

the modulation power from the reduced σ_{inho}, which only consisted of the inhomogeneous contribution to the BP spreading. From $P_{mod,m}$ in Table 4.4 it could be seen that the values for the lung TEPs and the balsawood were multiple times smaller than for the other materials. This showed that their heterogeneous effect on the BP was negligible, which was already discussed earlier (Section 4.1.4) and basis for $P_{mod,inho}$. The largest $P_{mod,m}$ was found for pumice. As it was the only material, which was not tissue like, it could not be concluded that the composition had an additional contribution to the MP. The second and third largest MP was found for the konjac sponge and the cork slabs, respectively. Both samples had macroscopic air holes in the order of mm, which seemed to affect the modulation power. In the column $P_{mod,inho}$ of Table 4.4 the modulation power was reduced by about 0.11 mm given in Equation 4.4. This expressed better the individual inhomogeneous contribution to MP for different materials.

Table 4.4.: Modulation Power for full material contribution and only inhomogeneous contribution

[mm]	$P_{mod,m}$	$P_{mod,inho}$
Lung TEP Inhale 7 cm	0.11	
Lung TEP Inhale 4 cm	0.12	
Lung TEP Inhale 2 cm	0.13	
Lung TEP Exhale 2 cm	0.09	
Cork 5.2 cm	0.61	0.50
Cork 2.5 cm	0.66	0.55
Cork Slabs	0.80	0.69
Balsawood	0.12	
Floral Foam	0.68	0.57
Konjac Sponge	1.06	0.95
Pumice	1.15	

4.1.5. Model for Calculations of the Longitudinal Bragg Peak Spreading

As described in section 3.7 it was tested if the voxel model could be modified to calculate the BP spreading based on the HU grid instead of a voxel grid. σ_m was calculated in two different approaches, once as the sum over all Hounsfield unit values HU_i along the beam path through the material

$$\sigma_A^2 = d^2 \cdot \sum_{i=1}^{n} \left(\frac{HU_i}{HU_{mat}} \right) \left(1 - \frac{HU_{mean}}{HU_{mat}} \right), \tag{4.8}$$

and once as the average HU values HU_{mean} of the HU_i times the number of voxels along the path in the material

$$\sigma_B^2 = d^2 \cdot n \cdot \frac{HU_{mean}}{HU_{mat}} \left(1 - \frac{HU_{mean}}{HU_{mat}} \right). \tag{4.9}$$

The HU_{mat} was derived from ρ_{mat}, which was assumed to be the (skeletal) density of the inhomogeneous materials, if they do not contain air cavities (see Webb [45]). The calculation was conducted by interpolation of the values of the CT conversion table (see appendix A.1) and were given in Table A.4 in the appendix. The results were shown in Table 4.5. The HU values were taken from the same CT scans, which were used for dose calculations in the TPS. Additionally, for the floral foam and the pumice older CT scans were available with a different resolution where the voxel size in beam direction was 2 mm. No calculation for the lung TEP were performed since the plates were considered homogeneous and no HU_{mat} could be given.

Table 4.5 showed that the effect, if Equation 4.8 or 4.9 was applied, was little. This

Table 4.5.: Calculation based estimation (σ_A and σ_B) of Bragg peak spreading compared to results from measurements σ_m

[mm]	σ_A		σ_B		σ_m
Voxel size in [mm^3]	1.17 x 1.17 x 1	0.68 x 0.68 x 2	1.17 x 1.17 x 1	0.68 x 0.68 x 2	
Cork 5 cm	2.97		2.98		2.88
Cork 2.5 cm	2.06		2.06		2.06
Cork Slabs	1.76		1.78		1.82
Balsawood	2.06		2.06		1.05
Floral Foam	1.63	2.37	1.63	2.37	1.18
Konjac Sponge	1.38		1.40		1.76
Pumice	2.03	2.83	2.03	2.82	3.20

proved that the ratio of HU_{mean} to HU_{mat} was more dominant than the HU variation HU_i in beam direction. Compared to the results from the IDD measurements σ_m, the results from the calculation of the 1.17 x 1.17 x 1 mm^3 voxel size agreed within 3 % percent for the cork samples. However, the other samples had a relative deviation between about 20 % to 100 %. The BP spreading of balsawood (96 %) and floral foam (38 %) was overestimated and of pumice (−37 %) and konjac sponge (−22 %) underestimated.

Moreover, the CT voxel size was a non-negligible influence factor for the results. For the 0.68 x 0.68 x 2 voxels d was 2 mm instead of 1 mm while the number of voxels n along the beam was halved. This resulted in a factor 2 for σ^2 or $\sqrt{2}$ for σ, which was the amount that σ increased from 1.17 x 1.17 x 1 to 0.68 x 0.68 x 2 voxel size. It was found that neither HU_{mean} nor HU_i changed considerable with the size of the voxel. This could be either a result of the voxel volume not being cubic (d^3 [mm^3]) or that HU_i could not represent the density variation well enough because the CT voxel size was much larger than the pore size of the material.

Another identified problem was the non-linearity of the HU to density calibration, which would be required for the initial assumption of $\frac{\rho_{mean}}{\rho_{mat}} = \frac{HU_{mean}}{HU_{mat}}$. It was also tested if the highest HU value (highest density) in the material would be sufficient as HU_{mat}, instead of deriving HU_{mat} from the true density ρ_{mat}. However, this overestimated σ_m by a lot since it would have required the pore sizes to be in a comparable size to the CT voxels.

In summary, the HU based BP spreading model was limited by many uncertainties and to estimate its applicability a much larger material variation would have been required, ideally with cubic voxel dimensions.

4.2. Measurements Transversal to the Beam Direction

4.2.1. Preliminary Investigations

In order to measure transversal to the beam line, data from IDD measurements were required to assure that the measurements were always taken at depths relative to the R_{80} position of the respective materials. At 97.4 MeV the beam width was broader and the gradient of the dose fall off lower. As small field detectors are sensitive to dose gradients, it was assumed that the measurements benefited from measurements at lower energies and an effect of a lateral beam spreading would then be easier to observe. The shape of the lateral profile depends on the depth in water, as indicated by Equation 2.22. Due to the range straggling caused by the materials the lateral profiles need to be obtained at a corresponding depth in water. The reference depth was chosen as the R_{80} of each tested material. Based on the R_{80} the ranges at 50 %, 80 %, 90 % and 97.5 % were calculated. As the smallest detector steps were 0.1 mm minor uncertainties were inevitable.

In order to verify the water reference R_{80} a 4 x 4 mm^2 field was irradiated and a depth dose profile was measured using the micro diamond chamber, which was then equivalent to an IDD measured with the BP chamber.

4.2.2. Lateral Beam Spreading

In Figure 4.12 the lateral profiles were displayed at 50 % and 90 % range of the R_{80}. In

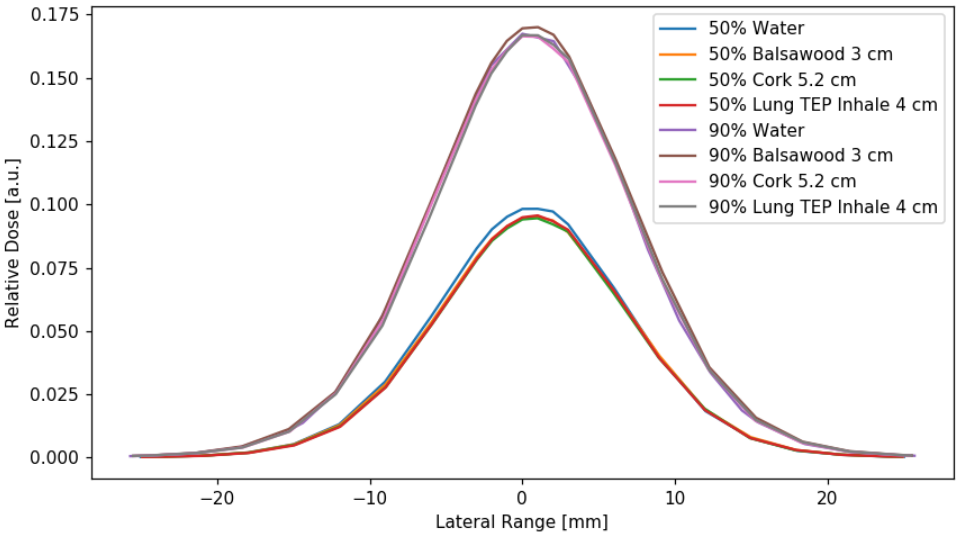

Figure 4.12.: Lateral profiles of different materials at 50 % and 80 % range of their corresponding R_{80}

order to evaluate the effect of a material on the lateral beam spreading the width of the

profile was derived at 50 % and 10 % of the dose maximum. The results were shown in Table 4.6 as the mean width and their standard deviation and in Table 4.7 as the relative deviation to the width to the water profile. The results showed no spreading of the beam for any material. The largest deviation was seen for the lung TEP with 2.5 %, which was considered as a range uncertainty due to different densities (see Section 3.3.1) of the used plates for range and lateral measurements. The deviations of the other two materials were almost always below 1 %.
Overall the uncertainties were small for all measurements and considered as setup instead of material effects on the beam. As the Gaussian fit gave very similar results for the FWHM and the width at 10 % was not shown in more detail.

Table 4.6.: Average width of the lateral profiles per range and material with their corresponding standard deviations in [mm]

[mm]	FWHM			
relative to R_{80}	50 %	80 %	90 %	97.5 %
Water	14.50 ± 0.02	14.89 ± 0.00	15.15 ± 0.01	15.24 ± 0.01
Lung TEP Inhale 4 cm	14.66 ± 0.00	15.27 ± 0.00	15.32 ± 0.00	15.48 ± 0.00
Cork 5.2 cm	14.50 ± 0.03	15.01 ± 0.03	15.35 ± 0.08	15.22 ± 0.01
Balsawood	14.46 ± 0.01	14.95 ± 0.01	15.11 ± 0.04	15.12 ± 0.07

[mm]	Width at 10%			
relative to R_{80}	50 %	80 %	90 %	97.5 %
Water	26.99 ± 0.06	27.97 ± 0.00	28.53 ± 0.01	28.58 ± 0.05
Lung TEP Inhale 4 cm	27.27 ± 0.00	28.46 ± 0.00	28.83 ± 0.00	28.80 ± 0.00
Cork 5.2 cm	27.15 ± 0.05	28.16 ± 0.03	28.61 ± 0.03	28.19 ± 0.16
Balsawood	26.94 ± 0.02	28.21 ± 0.05	28.57 ± 0.02	28.58 ± 0.00

Table 4.7.: Relative deviation (in %) to water of the average width of lateral profiles at 50 % and 10 %

in %	FWHM				Width at 10 %			
relative to R_{80}	50 %	80 %	90 %	97.5 %	50 %	80 %	90 %	97.5 %
Lung TEP Inhale 4 cm	1.1	2.5	1.2	1.6	1.1	1.8	1.1	0.8
Cork 5.2 cm	0.0	0.8	1.3	-0.1	0.6	0.7	0.3	-1.4
Balsawood	-0.2	0.4	-0.2	-0.8	-0.2	0.9	0.1	0.0

4.3. TPS Simulations

4.3.1. Integral Depth Doses

The simulations and the subsequent derivations were performed as described in Section 3.6.3.1 and the results of the TPS simulations were summarised in Table 4.8. Additionally to WET and σ_m, the FWHM of the Bragg curves were shown in Table 4.8. $\text{FWHM}_{wat+mat}$ was the width of the Bragg peak, where the water contribution to the BP spreading was not yet deduced. The FWHM_{wat} was the width of the reference BP within each CT image as described in Section 3.6.3.1. The average value of these water references was given as *Av. Water Reference* with the STD of the FWHM.

Table 4.8.: WET, σ_m and FWHM derived from simulations in RayStation with measurement results in parenthesis

[mm]	WET	σ_m	$\text{FWHM}_{wat+mat}$	FWHM_{wat}
		97.4 MeV		
Av. Water Reference		2.51 (2.61)	5.90 (6.14)	5.90 ± 0.11
Lung TEP Inhale 2 cm	3.34 (4.26)	1.08 (0.73)	6.36 (6.37)	5.83
Lung TEP Inhale 4 cm	7.68 (8.06)	0.71 (0.98)	6.07 (6.56)	5.83
Lung TEP Inhale 7 cm	13.57 (14.30)	0.78 (1.23)	6.15 (6.79)	5.86
Lung TEP Exhale 2 cm	10.03 (10.19)	0.31 (0.95)	5.86 (6.53)	5.82
Cork 5.2 cm	13.46 (13.65)	1.25 (2.88)	6.80 (9.14)	6.14
Cork 2.5 cm	6.37 (6.42)	0.85 (2.06)	6.27 (7.82)	5.95
Cork Slabs	3.72 (4.13)	1.60 (1.82)	6.88 (7.48)	5.83
Balsawood	8.82 (8.90)	– (1.05)	**5.91** (6.62)	**5.98**
Floral Foam	0.14 (2.05)	1.01 (1.18)	6.46 (6.73)	6.00
Konjac Sponge	2.40 (2.92)	1.05 (1.76)	6.32 (7.41)	5.80
Pumice	14.08 (8.86)	0.33 (3.20)	6.03 (9.71)	5.98
		148.2 MeV		
Av. Water Reference		5.13 (5.35)	12.08 (12.60)	12.08 ± 0.11
Lung TEP Inhale 4 cm	8.54 (8.65)	– (0.93)	**12.08** (12.79)	**12.11**
Cork 5.2 cm	13.41 (13.63)	1.67 (2.87)	12.81 (14.30)	12.19
Cork 2.5 cm	6.32 (6.43)	0.39 (2.08)	11.96 (13.52)	11.93

The WET, compared to the measurement values in parenthesis in Table 4.8, showed that the difference was less than 1 mm for most samples except for the floral foam and the pumice.
The floral foam had an average HU value of −978. In the HU to density calibration table (see Table A.1) all HU values below −980 were automatically set to air density, therefore, not the whole floral foam was considered in the dose calculation and the WET

was underestimated. This HU threshold affected the konjac sponge as well, although to a smaller extend as its HU spectrum was wider.
On the opposite the pumice was overestimated by more than 5 mm. From the average HU of pumice in Table 4.3 it could be seen that a density of about 0.35 g/cm^3 was assigned via the conversion table (Table A.1 in the appendix). This was a consequence of pumice being not tissue like and lead to the miscalculations in RayStation.
The simulations of the TEPs were not based on CT scans of the material but were obtained from self drawn structures in an "empty" CT image and uncertainties due to physical measurements and reproduction of those on the computer could not be excluded. Therefore, a comparison of measurement and RS results was not possible as the uncertainties were expected to be in the same order of magnitude as the difference between measurement and RS results.
For the remaining materials, namely the 3 cork samples, the konjac sponge and the balsawood, the largest deviations between the WET obtained from RayStation and the measurements were for the konjac sponge and the cork slabs, which were under about 0.5 mm and had the largest inhomogeneities of all tested materials excluding the pumice. Even when all setup uncertainties for the measurements, CT scans and treatment planning were considered to $0.2 - 0.3$ mm, this differences between measurement and RS were relevant.

In Table 4.8, no value for the BP spreading σ_m of balsawood and the lung TEP inhale 4 cm was given. By comparing their respective FWHM$_{wat+mat}$ and FWHM$_{wat}$ it could be seen that the BP width of the reference measurement was larger than the BP width with additional material in the beam path.
The different BP widths of water FWHM$_{wat}$ in different CT images showed that their determination had an uncertainty of a few hundred µm and a STD of 0.11 mm. The same uncertainty was assumed for the FWHM$_{wat+mat}$. From these cumulative uncertainties it happened that the FWHM of only water appeared larger than with additional balsawood and 4 cm lung TEP at 148.2 MeV in the beam path.

The uncertainties were a consequence of the difficulties of determining the precise value of the peak maximum. Due to the 1 mm resolution of the dose grid in RS, the maximum of the BP was accurate within 1 %, which propagated to an uncertainty of 1 % of the proximal and distal R_{50} position and consequently of the STD of the FWHM as stated above.

A BP spreading, which was larger than the uncertainties, could only be seen for $\sigma_m > 0.7$ mm, which corresponds to an approximate FWHM difference of 0.2 mm. This also displayed the sensitive nature of small σ_m's, which varied considerably for small variations of the FWHM, when FWHM$_{wat}$ and FWHM$_{wat+mat}$ were comparable within $1 - 2$ %. For example, σ_m of pumice was 0.33 mm, while the difference in the FWHM was only 0.05 mm.
With the present uncertainties in σ_m for the RS data a conclusive comparison to the

measurements with this IDD property could not be given. Although, by comparing the FWHM of measurements with RS, it was seen that the BP spreading was constantly underestimated by the TPS. This was valid not only for homogeneous and heterogeneous materials but also for the water reference measurements. Even if the water discrepancy of 0.25 mm at 97.4 MeV and 0.52 mm at 148.2 MeV was considered, the BP spreading was still considerable underestimated for all materials.

4.3.2. Lateral Profiles

The TPS simulations were done for the 5.2 cm yoga cork as the highest possible effect was expected from looking at the measurements (see 4.1). The determination depth for the lateral profiles with sub-millimetre accuracy, as used in the experiments, was not possible due to the 1 mm voxel resulution in sagittal (beam) direction.

In Figure 4.13 a RayStation line dose of the lateral profiles for cork and water was displayed. The lateral profiles were obtained at a depth parallel to the maximal dose value calculated by RS. For determining the FWHM and the width at 10 % of the

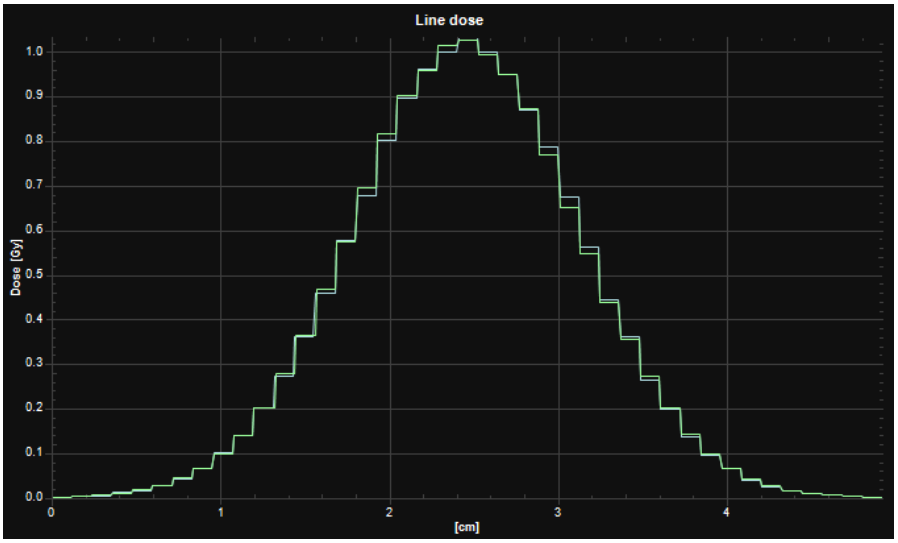

Figure 4.13.: Line Dose in RayStation of lateral profile for cork and water

maximum the same functions had been used as for the measured lateral profiles. The FWHM of water was 15.49 mm and 15.40 mm for cork, which corresponds to a relative deviation of -0.58 % compared to respective measurements. The width at 10 % was 28.42 mm (water) and 28.43 mm (cork), which corresponds to a relative deviation from the measurements of 0.04 %. As expected from the measurement data also in the TPS simulation no effect on a lateral beam width of the inhomogeneities could be found in the observed materials.

5. Discussion

5.1. Lung Substitutes

One of the main objectives of this thesis was to investigate the RiFi effect of different lung substitutes on the BP. Finding suitable surrogates was a difficult task itself. This was still preferred over the usage of a real lung due to several reasons:
The living tissue changes its structure upon death. The loss of internal pressure causes a deflation of the lung, which could partially be compensated by artificial inflation. However, from investigations of Markel et. al. [52] of a swine lung it was concluded that an uniform inflation was not possible and differences to human lung were observed. Further, the amorphous and soft structure a of lung complicates the reproducibility of measurements with static positions. Measurements of a plastinated human lung by Titt et. al. [43] demonstrated the position sensitivity and its effect on the proton beam. For investigating the capability of the TPS to deal with inhomogeneous tissue in the dose calculation process, the dose measurement alone would have been insufficient and the overall uncertainties resulting from the repeated setup for CTs and measurements were considered as too prone to errors.

The decision basis for the selected materials was given in Section 3.3. In prior works a large number of different lung substitutes were investigated. For example, Mayer et. al. [53] investigated breakfast cereals, pretzels, oregano, bean bags or saw dust as suitable lung tissue substitute. Ringbæk et. al. [47] tested different synthetic foams, such as polyurethane, polystyrol or foam paddings, and Titt et. al. [43] used a 3D printed phantom. The choice of materials in this thesis was influenced by these works. The aim was to look into alternatives which have not already been investigated, because prior tested materials could not mimic the porous structure of lung tissue. For example, polystyrol was found to be homogeneous, which made it a less suitable lung substitute candidate, instead the floral foam was chosen for investigation.
A number of candidates were considered but lastly declined. One of those was a natural sponge, which was barely visible in a CT image because of its low density. Also various food was discussed, such as bread or bakeries, which were declined due to their limited preservability and fluid loss. Dry candidates, such as rice or caraway, came along with the problem that they needed a container, which would have been present in the measurements and the CT scans.

From the perspective of mimicking the properties of real lung, each sample had its own characteristics and drawbacks.

The lung TEPs had inconsistent densities (see Section 3.3.1), which affected the results considerably and their homogenous structure made them unsuitable to investigate the RiFi effect of lung tissue on the proton beam even the composition was most equivalent to real lung tissue comparing to the other materials. Even though, it should be mentioned that the TEPs were designed to be used as reference material for a HU-density calibration and its subsequent validation and not to simulate BP spreading.
The yoga cork samples gave one of the most reliable and consistent results. Differences for the normalised WET and σ_m between the Yoga blocks with different width were considered as local variations of density within the material. Further, it was not clear if air filled pores lead to the BP spreading or a variation of density from grain to grain in the material. The cork slabs on the other side had macroscopic air cavities, which might be comparable to bronchi in a lung and were therefore considered to be suitable to investigate the BP spreading.
The balsawood was similar homogeneous in the measurements as the lung plates. In the CT image, the HU variations and therefore density variations were visible due to annual rings of the wood. It was assumed that a high gradient of the stopping power between neighbouring voxels was required for an inhomogeneous BP spreading. However, this was not the case for the annual ring in the balsa wood, where the gradient was low and varied rather steadily (see CT image in the appendix, Figure A.5). These annual rings could be the reason for the discrepancy of the WET (normalised to the same thickness) compared to the other materials (see Section 4.1.3.1), which relied on an average density distribution of the whole sample. In the end, balsawood was as unsuitable as lung substitute as the lung TEPs for the purpose of this thesis, but it should be noted that the investigated sample had a density of about 0.33 g/cm^3, which was considerable high for typical balsawood and other, less dense samples might have a more heterogeneous structure.
Floral foam measurements displayed a relatively large BP spreading, if its density was not considered (normalised thickness or modulation power). However, the density could normally not be modified in opposite to the width and was not comparable to lung, which made it unsuitable as a substitute.
The konjac sponge was similar to the floral foam but with higher density and a larger BP spreading, although the density was still much lower than the one of a real lung. It was discussed to fill the konjac sponge with water to increase its density, which would have also shifted its HU spectrum, which was best comparable to real lung. However, a similar experiment was conducted by Fuse et. al. [54], who reported difficulties in a homogenous water distribution and in keeping the amount of water in the material constant. The konjac sponge gave the highest modulation power of all tissue like materials. From CT image and by visual evaluation of the sponge, it could be seen that the air cavities were smaller on the outside than on the inside. The konjac sponge had therefore two types of inhomogeneities: one for the mass difference between fibre and air, which was rather constant, and one for the different amount of the volume occupied by fibre or air, respectively, which was position dependent. This “double inhomogeneity” argument could be used for the cork slabs as well and was a likely reason for their larger

BP spreading in comparison to the yoga cork. Overall, the konjac sponge was assumed to have the largest uncertainties of the measured WET and σ_m. The material could not be mechanically machined and needed to be cut and polished by hand resulting in uncertainties of determining its density, width and realise its surfaces to be parallel to each other. For higher quality results with lower uncertainties, larger sponge samples would be required.
Pumice is no lung substitute. Its lack of light atoms, such as hydrogen or carbon, clearly disqualified it, what was especially pronounced in the TPS investigations (see Section 4.3.1) by the improper HU to density conversion. If used as any substitute it might be useful as porous bone substitute. Ringbæk et. al. [47] investigated materials for their usability as simultaneous range shifter and ripple filter in carbon beams. In this context, the pumice could be an interesting candidate. However, both suggestions are out of scope of this thesis.

5.2. Integral Depth Dose Analysis

5.2.1. Measurement Uncertainties

The measured integral depth dose values were fitted by polynomial function to obtain the values at certain POIs. This was motivated by the fact that the measured IDDs showed an uncertainty depending on the delivered amount of particles per measurement point, referred to as wobbling in Section 3.6.1. Usually two data points were obtained per spill ($\sim$ 5 s) and the uncertainty could therefore be related to the variation of the beam intensity during the spill or the movement of the detector. The deviation of the measurements at dedicated POIs between the linear interpolation utilised by the PTW MEPHYSTO software and the fit functions were in the order of tenth of µm.
According to the manufacturers specifications of the MP3-PL water phantom, the positioning accuracy was about 0.1 mm. Consequently, it was debatable if a presentation of data to the second decimal was necessary. However, the standard deviation of measurements within the same measurement session was below 0.1 mm and uncertainties larger than that resulted from uncertainties in the reproducibility of the setup in different measurement sessions. The largest source of uncertainty within a measurement session was eliminated by evaluating only data for one detector movement direction and avoiding hysteresis effects. The absolute position of the Bragg peak differed by $0.05 - 0.13$ mm measuring in up or downstream direction. For the FWHM, which was used to derive the BP spreading, no directional dependence of the detector movement nor its position in the water phantom was observed and the differences in width were below 0.05 mm. For absolute range measurements the largest uncertainty resulted from difficulties at determining the first point of measurement with about 0.5 mm between different measurement sessions. Those did not affect the results, because absolute ranges were not evaluated. Temperature effect of the water which influence the density were considered but smaller than 0.01 mm. All measurements took place at water temperatures between 20.8 and 21.2 °C.

In summary, the absolute range uncertainties were up to 0.5 mm for the R_{80} in water in different measurement sessions, but the relative range uncertainty was below 0.1 mm justifying the data presentation with the second decimal as ranges were evaluated relatively to each other.

5.2.2. IDD Properties

In addition to σ_m the penumbra of the BP between the R_{80} and R_{20} was investigated as quantity of the BP spreading. The penumbra was used in literature [30, 31, 43, 49] when, instead of a single PB, the inhomogeneous tissue effect was investigated with a SOBP or the focus was to emphasise how large the region was, which received additional dose. For normalisation of the penumbra to the same width the natural logarithm worked best, but showed an energy dependence. This was a consequence of the contribution of water to the penumbra which could not be excluded the same way as for σ_m (see Equation 3.5). The utilisation of both σ_m and the penumbra to determine the BP spreading seemed redundant especially since σ_m proved to be superior for material property investigations.

The acquisition of σ_m by deriving it from the proximal and distal R_{50} was a straight forward and fast approach. It gave precise results, but as seen for the TPS results, was fragile if the BP maximum and consequently the R_{50}'s could not be exactly located. In this case due to a resolution limited by the dose grid, but it would also be unsuitable if a BP had a dented and therefore not pronounced maximum. For such scenarios the approach of fitting of a Gaussian convolution to the water reference as seen in the work of Witt [48] and successive works is favourable.

The normalisation of WET and σ_m was necessary to compare different aspects of the materials with each other. σ_m normalised to the same thickness 1 g/cm^2 was closely related to the modulation power and only differed by the composition and the uncertainties in the determination of the thickness. Normalising σ_m^2 to the same WET of 1 mm would by definition give the modulation power of the material (see Equation 4.6). Consequently, it would have been possible to use the $P_{mod,m}$ in Section 4.1.4.2 instead of σ_m in thickness normalisation, which would lead to a linear relation between $P_{mod,m}$ and HU_{range}.
Witt derived a modulation power for real (swine) lung tissue in a range between 0.35 to 0.74 mm. This agreed best with the modulation power of the yoga cork and the floral foam making them the most realistic lung substitutes in terms of heterogeneity.

5.2.3. Voxel Model

The motivation of this concept was to extend the theory of (homogeneous) BP spreading by including heterogeneity effects of the material. The base form of the BP spreading was derived from a binomial distribution (described in Section 3.7) and was given by

$$\sigma^2 = d \cdot W(p - p^2). \tag{5.1}$$

Generally, the voxel model only applies for uniform distributed voxels with cubic shapes and cannot be applied easily in reality. Realistic materials do not have a binary density and distinguishable interfaces. In addition, realistic materials usually have homogeneous larger scale structures in the order of millimetres such as blood vessels in lung tissue. In contrast to sub-millimetre heterogeneities, those larger scale structures contribute differently to the BP spreading as discussed by Schaffner et. al. [55]. In order to extend the binary voxel model to realistic materials, it could be beneficial to replace the voxel size with a parameter, which describes the length and gradient of the variation of density, respectively stopping power.
Those conclusions were motivated by evaluating the results of the HU based voxel model in Section 4.1.5. The HU based model was affected by the non strict linearity between density and HU value. For balsawood the BP spreading was largely overestimated. This was likely due to the fact that the probability p was not 1 (homogeneous) even when the neighbouring voxels had the same HU value and consequently their contribution to σ_{inho} should have been negligible. However, this was intended because it was assumed that a fine structure was not displayed in the CT image, which raised the question about the amount of fine structure relevant for the BP spreading.
Summarised, the voxel model adapted to HU could not represent the straggling of the BP good enough to be applicable. Also the number of tested materials was not high enough to be representative.

5.2.4. Hounsfield Unit Spectrum

The HU spectrum was used to derive the range of different HU in a material. A 2σ confidence interval was chosen to include most of the values but still exclude HUs which were created by artefacts or other disturbances in the material. In relation to the beam width (see Section 4.2.2) a 2 x 2 x 2 cm^3 box size was chosen. Especially for balsawood it was found that the box size correlated with the HU_{range}. This lead to the conclusion that not only the overall variation of HU values was important but also their local distribution. Its effect on the BP spreading was discussed in the voxel model (Section 5.2.3) already. For HU values or densities without larger scale patterns, such as for the homogeneous TEPs or the corks, the HU_{range} could be applicable to describe the BP spreading (see Figure 4.11), under the assumption that the density variation was reflected in the CT image. This was not the case for the floral foam. Its low density and consequent low contrast to air and equally distributed heterogeneous structure made the foam appear more homogeneous than it was in the measurements. Why the pumice had a large BP spreading at a rather small HU_{range} was not clear. It could be that the material is not properly displayed in the CT or that the larger stopping power ratio between stone and air was not reflected by the HU_{range}.
As discussed in the IDD properties (Section 5.2.2), instead of σ_m normalised to thickness 1 g/cm^2 it would have also been possible to use the modulation power to investigate the HU_{range} - BP spreading relation in Section 4.1.4.2. As the range of HU should be independent of the homogeneous BP spreading it seemed reasonable to compare the HU_{range} to $P_{mod,inho}$. However, this was not worthwhile to be investigated as not enough

different materials were available.

5.2.5. RayStation and Comparison to Measurements

In Section 4.3.1 it was already outlined that the Monte Carlo dose simulation in RayStation is capable of predicting the range, respectively the WET correctly from CT scans for homogeneous as well as for heterogeneous materials. The exceptions were the floral foam and the pumice in which cases an explanation was given. España and Paganetti [56] reported range uncertainties of the 90 % dose level in the distal fall off of a SOBP in the order of mm due to limited CT resolution of heterogeneous structures. Such uncertainties could not be verified in the setup frame of this thesis.

The calculation of the BP spreading σ_m was complicated by the resolution of the dose grid, which cannot be set smaller than 1 mm, and the large uncertainty of the proximal R_{50}. A 1 % uncertainty in determining the maximum of the BP propagated to a change of the R_{50} by about 0.15 mm at 97.4 MeV and about 0.30 mm at 148.2 MeV. This uncertainty could be one of the reason for the underestimation of the FWHM of water in the results from the TPS. Determining the maximum was also the most difficult fit task. From all tested polynomials and a Gaussian, the second order polynomial proved to be most accurate. Further only 3 data points were considered in the fit. These were chosen in a way that the expected maximum was between first and second and the third to be to the right of the other two, respectively in the penumbra. Although 1 % uncertainty was inevitable the fit was superior to interpolation. If the POIs were obtained by interpolation, the highest dose point would have been considered as the maximum, which would have lead to an underestimation of the maximum by up to approximately 10 %.
All uncertainties aside, the results of the derived FWHM from the TPS showed a notable underestimation of the BP spreading for the homogeneous materials and even more for the heterogeneous materials compared to the measurements. This showed that the RS MC dose engine (v4.1) was not capable to adequately calculate the straggling of the Bragg peak based on the CT image provided.
It is noted that RaySearch is aware of the underestimation of the BP spreading and in October 2018 patented a model[1] similar to the voxel model. It is supposed to override the homogeneous density information in a CT, for example lung tissue, to tackle the problem discussed here.

5.3. Lateral Profile Analysis

5.3.1. Measurements

In Section 4.2.2 the results for the measurements of the lateral beam spreading were shown. The lateral FWHM of the Bragg peak was not notably changed by putting some

[1] WIPO International Publication Number: WO 2018/189364 A1

material in the beam path. The deviations in Table 4.7 were rather a consequence of uncertainties resulting from the detector setup, the fitting curves or the predicted depths, where the profiles were measured, than any effect of additional material in the proton beam.
The largest differences in the lateral profile width between water and the materials were measured for the lung inhale TEP and were between $0.8-2.5$ %. The major uncertainty was due the choice of the TEPs stacked to 4 cm width, which were used for IDD measurements and lateral profile measurements and differed in density (see Section 3.3.1). This introduced an error in the range estimation by about 0.4 mm propagating in an offset of the width of the lateral profiles.
For the cork sample and the balsawood the relative deviations to water were below 1.4 % and did not show any correlation pattern. They appeared to be a sole consequence of measurement uncertainties as the width of the lateral profile depended on the relative R_{80}'s of the materials.

In conclusion, no lateral beam spreading was measured. This confirmed findings from Russell et. al. in 1995 [57], who argued that heterogeneous materials with similar composition to tissue or water would result in the same angular distribution as long as the range was correctly determined. Consequently, this argument excluded bone tissue. For heterogeneous bony structures, Sawakuchi et al. [31] showed with MC simulations an effect of the size of the heterogeneities to the angular distribution. The effect was indirect proportional to the voxel size of the inhomgeneities, ranging from 50 mm (homogeneous) to about 0.8 mm. This motivated the lateral measurements in this thesis. The 97.4 MeV proton energy was chosen, because a lower energetic beam had a larger beam width. Consequently the lateral dose fall off had a smaller gradient, which was beneficial for the detector accuracy and spreading effects would then have been easier to measure. However, in the chapter 46 of Mayles [5] it was argued that a narrow beam (< 10 mm) with about 100 MeV would lead to a disappearance of the BP due to a lack of lateral scatter equilibrium. In reverse, this scatter equilibrium might had smeared out any heterogeneity effect for pencil beams wider than 10 mm after a certain distance in water. Nevertheless, if the material inhomogeneities had an effect on the lateral beam profile so small that it was not detected in the measurements, it would be negligible for clinical considerations.

5.3.2. RayStation and Comparison to Measurements

To determine lateral profiles from TPS simulations was difficult, since the FWHM depends on the range. As discussed above already a range uncertainty of 0.4 mm leads to measurable errors, however, the highest voxel resolution in RS was 1 mm. The only reasonable range for which comparable profiles were acquired was at the depth of the dose maximum. The TPS results in Section 4.3.2 showed that the lateral beam widths were fairly similar and their differences a consequence of the fit uncertainty.

The lateral measurement results, which were closest related to the TPS results, were for the 97.5 % range. Technically a solution would have been to calculate the width for lateral profiles in different depths and interpolate the data to the desired depths. However, the range uncertainties in the measurements would persist and the trade off to reduce the TPS range uncertainty seemed unnecessary. The absolute and relative deviation of the measurement from the TPS results in Table 5.1 showed that the width of the profiles were similar and the deviation in the order of the measurement uncertainty.
This proved that the MC dose engine of RayStation calculated the lateral profile of homogeneous water and inhomogeneous cork correctly for a single pencil beam.

Table 5.1.: Absolute and relative deviation of lateral profile width between TPS simulations and measurements

	FWHM		Width at 10 %	
	mm	%	mm	%
Water	-0.25	-1.6	0.17	0.6
Cork 5.2 cm	0.08	0.5	-0.24	-0.8

6. Conclusion and Outlook

The aim of this thesis was to test the influence of different materials, which had physical properties mimicking different aspects lung tissue on the proton beam characteristics. Their effects on a proton beam were quantified and compared to the predictions of the Monte Carlo dose engine v4.1 implemented in the treatment planning system RayStation. The heterogeneous texture of cork, konjac sponge, pumice and floral foam did not affect the range of the beam in water. In spite of this, it lead to a spreading of the Bragg peak in longitudinal direction, additionally to the spreading caused by homogeneous materials but not in lateral direction. This contribution of structure heterogeneities to the BP spreading, referred to as ripple filter effect, was a consequence of a density variation within the material which influence the proton path. Those variations in the µm range were not represented in the CT and the results showed that the TPS underestimated the BP spreading in its dose calculations leading to an overestimation of the dose maximum and an underestimation of dose in the fall off regions of the BP. The BP spreading caused by the inhomogeneities was $2-3$ times larger than the one of homogeneous materials and increased σ by up to 2 mm. Heavy ion beams, such as carbon, have a narrower BP and the dose determination/prediction uncertainties caused by the heterogeneity effect need to be investigated. The most realistic lung substitutes were the cork samples and heterogeneity effects on the carbon beams should be studied with this material, if possible with additional samples with different densities but a similar structure and elemental composition. Further investigations will also focus on applying corrections in the dose calculation process to consider heterogeneous structure effects on the particle beam.

A. Appendix

Table A.1.: CT Hounsfield units to density conversion according to MedAustron scanning protocol "Ad_Abdn"

HU	density [g/cm^3]
-980.8	0.001214
-810.8175	0.195
-499.4975	0.51
-67.365	0.96
-43.98	0.991
-6.745	1
39.41	1.062
216.4225	1.161
867.465	1.53
1283.35	1.82
2972	2.8
3070	7.6519

Table A.2.: List of all completed measurements

	Session 1	Session 2	Session 3
IDD			
97.4 MeV			
Water	u **d** u	**d** u **d**	**u** d **u**
Lung TEP Inhale 2 cm	**d** u **d**		
Lung TEP Inhale 4 cm	**d** u **d**		
Lung TEP Inhale 7 cm		**d** u **d**	
Lung TEP Exhale 2 cm	**d** u u		
Cork 5.2 cm	**d** u **d**	**d** u **d**	
Cork 2.5 cm			**u u**
Cork Slabs 2.4 cm			**u u**
Balsawood			**u u u**
Floral Foam	**d** u **d**		
Konjac Sponge			**u u**
Pumice	**d** u **d**		
148.2 MeV			
Water		**u** d **u**	**u** d **u**
Lung TEP Inhale 4 cm			**u u**
Cork 5.2 cm		**u** d	
Cork 2.5 cm			**u u**
Lateral Profile			
97.4 MeV			
Water			**h h**
Lung TEP Inhale 4 cm			**h**
Cork 5.2 cm			**h h**
Balsawood			**h h**

The table lists all performed measurements in all measurement sessions. The definition u and d indicate the relative detector movement to the propagation direction of the proton beam. Letters in bold highlight the measurements used for data evaluation.
d ... downstream (surface to depth); u ... upstream (depth to surface); h ...horizontal (left to right)

Table A.3.: Atomic composition of materials

	Atomic composition in % of mass fraction												
	H	C	N	O	P	Na	Al	Si	S	Cl	K	Ca	Fe
Real Lung[a]	10.3	10.5	3.1	74.9	0.2	0.2		0.3	0.3	0.2			
Lung Exhale TEP[b]	8.9	66.0	2.4	20.4						0.6		1.7	
Lung Inhale TEP[b]	9.8	67.5	3.5	18.6						1.6			
Cork[c]	7.7	56.6	0.4	34.5				0.7			0.1		
Balsawood[d]	6.0	50.0	1.0	43.0									
Floral Foam[e]	5.0	69.0	9.0	16.0									
Konjac Sponge[f]	6.0	37.0	7.0	49.0					1.0				
Pumice[g]				62.0		1.8	5.9	25.3			0.9	0.6	0.4

Sources for atomic compositions of different materials:
[a] Real lung: as given by Schneider et. al. [32]
[b] Lung TEP: as stated by the producer CIRS (USA)
[c] Fuse, H., Fujisaki, T., Ikeda, R., & Hakani, Z. (2018). Applicability of Lung Equivalent Phantom Using the Cork with Absorbed Water in Radiotherapeutic Dosimetry. International Journal of Medical Physics, Clinical Engineering and Radiation Oncology, 7(01), 27.
[d] `http://www.holzwurm-page.de/holz/holz/chemisch.htm`
[e] US patent no. 4,225,679; composition of phenolic resin assumed similar to polyurethane `https://en.wikipedia.org/wiki/Polyurethane`
[f] assumed to be comparable to natural sponges: Simpson, T. L. (2012). The cell biology of sponges. Springer Science & Business Media.
[g] `https://hesspumice.com/pumice-pages/why-pumice/superior-quality-pumice.html`

Table A.4.: Width, densities and theoretical Hounsfield units, if inhomogeneous materials did not contain air

	width W [cm]	mean density ρ_{mean} [g/cm^3]	skeletal density ρ_{mat} [g/cm^3]	theoretical HU $HU_{mat}(\rho_{mat})$
Lung (ICRU 44)		0.260	1.050[a]	
CIRS Lung Exhale TEP	1.01	0.502		
CIRS Lung Inhale TEP (higher density)	1.01	0.212		
CIRS Lung Inhale TEP (lower density)	1.00	0.198		
Cork 5.2 cm	5.17	0.266	1.150[b]	199
Cork 2.5 cm	2.48	0.266	1.150[b]	199
Cork Slabs	2.37	0.177	1.150[b]	199
Balsawood	2.98	0.327	1.500[c]	815
Floral Foam	7.45	0.029	1.150[d]	199
Konjac Sponge	3.35	0.092	1.150[e]	199
Pumice	4.06	0.241	2.350[f]	2130

The skeletal densities are based on assumptions from various sources listed below:
[a] deflated lung [32]
[b] González-Hernández, Florentino & Gonzalez-Adrados, Jose Ramon & García de Ceca, Jose & Sánchez-González, Mariola. (2014). Quality grading of cork stoppers based on porosity, density and elasticity. European Journal of Wood and Wood Products. 72. 149-156. 10.1007/s00107-013-0760-x.
[c] Stamm, A. J. (2002). Density of wood substance, adsorption by wood, and permeability of wood. The Journal of Physical Chemistry, 33(3), 398-414.
[d] in liquid form: `https://www.google.com/url?sa=t&rct=j&q=&esrc=s&source=web&cd=5&ved=2ahUKEwjc04_J-67hAhWllIsKHU9lAw4QFjAEegQICBAC&url=http%3A%2F%2Fwww.ucp.ru%2Fcommon%2Fimg%2Fuploaded%2Ffiles%2FPhenix_140Me.doc&usg=AOvVaw19lWWFg4ZS567IUnJRo3GF`
[e] based on the assumption of floral foam
[f] `https://hesspumice.com/pumice-pages/why-pumice/superior-quality-pumice.html`

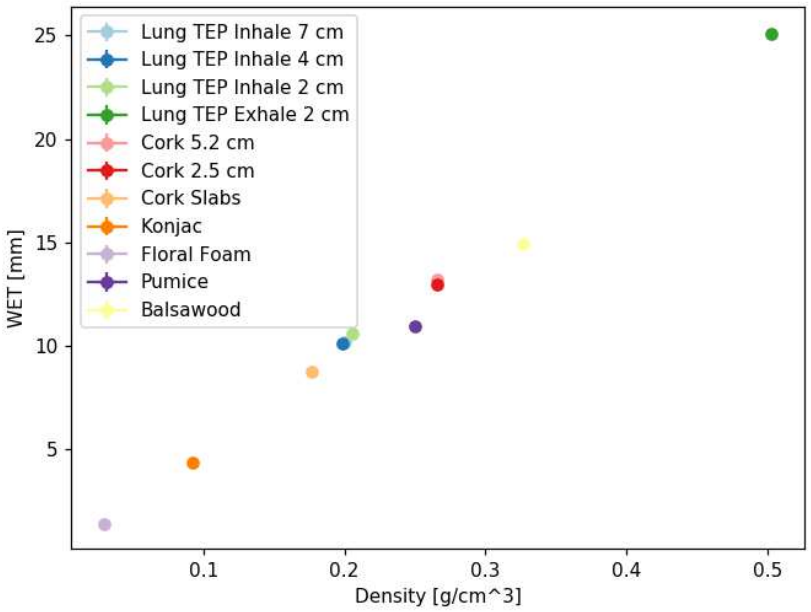

Figure A.1.: Density - WET for material width normalised to 5 cm

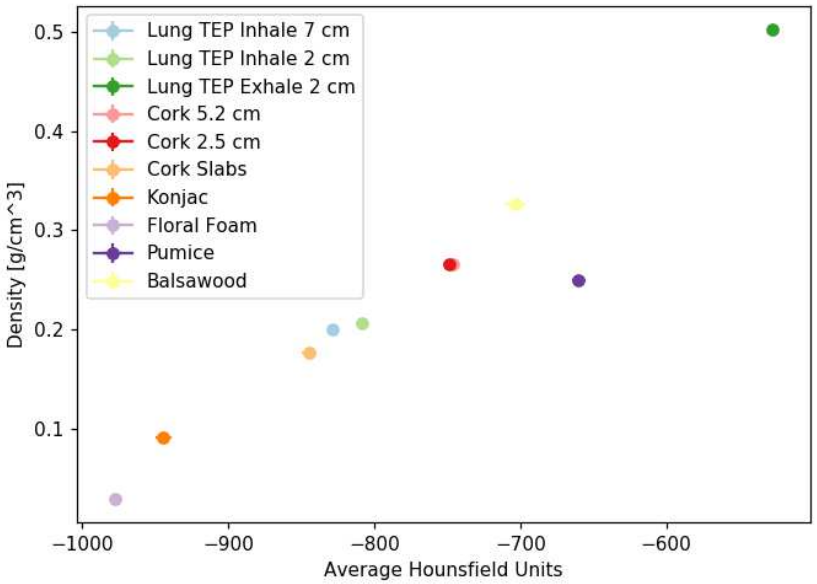

Figure A.2.: Average HU - density for material width normalised to 5 cm

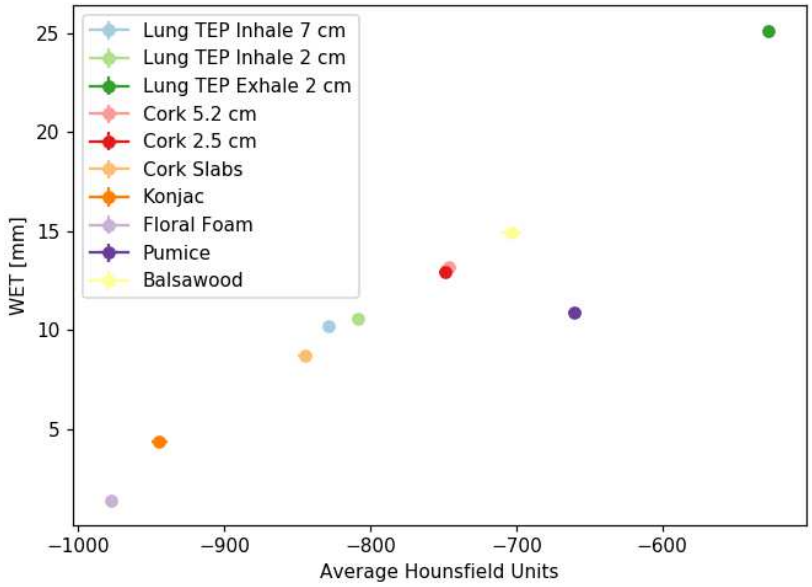

Figure A.3.: Average HU - WET for material width normalised to 5 cm

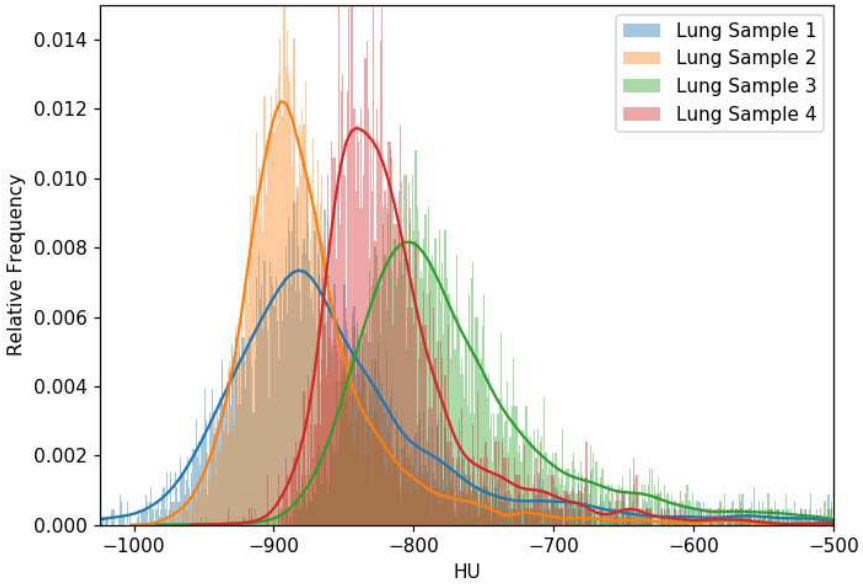

Figure A.4.: Hounsfield unit spectra of 4 different lung CTs with threshold above −500 HU

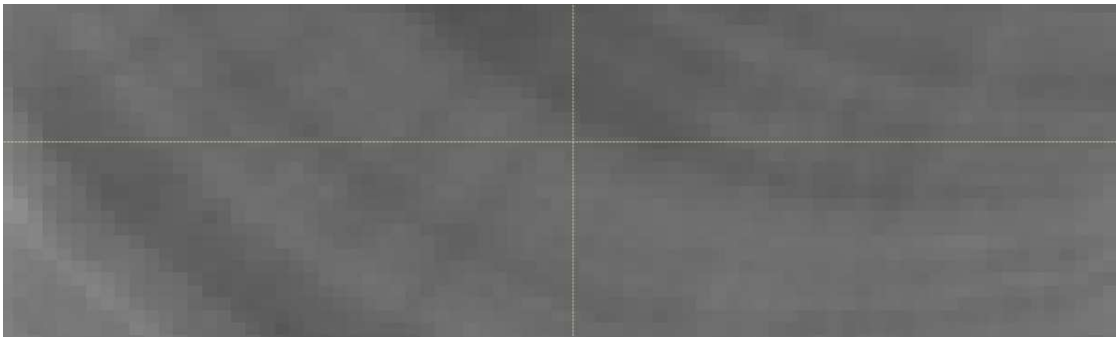

Figure A.5.: CT image of balsawood with visible annual rings and proton beam passing in vertical direction of the hair cross (pixel size 1.17 x 1.17 mm^2)

List of Figures

List of Tables

List of Abbreviations

BP	Bragg peak
CT	Computer tomography
CBCT	cone beam computer tomography
DICOM	digital imaging and communications in medicine
ECR	electron cyclotron resonance
FWHM	full width half maximum
HU	Hounsfield unit
IBT	ion beam therapy
IDD	integral depth dose
IMRT	intensity modulated radiotherapy
LET	linear energy transfer
LINAC	Linear accelerator
MC	Monte Carlo
MCS	multiple Coulomb scattering
MP	modulation power
MRI	magnetic resonance imaging
NSCLC	non small cell lung cancer
OAR	organs-at-risk
PET	positron emission tomography
PB	Pencil beam
PMMA	polymethyl methacrylate
POI	point of interest

RFQ radio frequency quadrupole

RBE relative biologic effectiveness

RiFi ripple filter

RS RayStation

SCLC Small cell lung cancer

SOBP spread out Bragg peak

STD standard deviation

TEP Tissue equivalent plates

TPS treatment planning system

WET water equivalent thickness

List of Variables

A_t	mass number of the traversed medium/target
$\vec{\mathbf{A}}$	surface
b	distance between charges
B	magnetic field
c	speed of light
$\frac{C}{Z_t}$	shell correction
d	pore size, voxel size, photon path length
D	Dose
e	elementary charge
E	energy
$\vec{\mathbf{E}}$	electric field
f	frequency
F	(Lorentz) force
I	mean ionisation energy, photon beam intensity, interval of the fit function
k	number of filled voxels in a line
m	particle mass
n	number of voxels in a line
n_e	electron density
N_A	Avogadro constant
p	momentum, probability of filled voxel, fit parameter
$P(k)$	binomial distribution
$P(\theta)$	lateral distribution
r	radius
R	range in water
s	free path length
S	stopping power
t	thickness [g/cm^2]
T	scattering power
v	velocity
V	volume
W	width of materials in beam direction [mm or cm]
Z_t	atomic number of the traversed medium/target
Z_p	atomic number of the traversing particle

β	ratio of v to c
δ	density/polarisation correction
ϵ_0	electric constant
ζ	radiological depth
θ	scatter angle
μ	linear photon attenuation, expected value/range shift of the Gaussian function
ρ	density
σ	Bragg peak spreading, energy straggling, standard deviation of the Gaussian function
Φ	lateral fluence

Bibliography

[1] J. Costa, "Cancer." Encyclopædia Britannica, inc. https://www.britannica.com/science/cancer-disease, May 2019. [accessed 23.07.2019].

[2] K. R. Aigner and F. O. Stephens, *Basics of Oncolgy*. Springer, Berlin, Heidelberg, 2 ed., 2016.

[3] U. Linz, *Ion Beam Therapy - Fundamentals, Technology, Clinical Applications*. Springer, Berlin, Heidelberg, 1 ed., 2012.

[4] D. Georg, "Introduction and basics of (medical) radiation physics." Basic Seminar: Medical Physics VIII - Physical Fundamentals of Radio Oncology, Medical University of Vienna, 2019.

[5] P. Mayles, A. Nahum, and J. C. Rosenwald, eds., *Handbook of Radiotherapy Physics*. CRC Press, 2007.

[6] N. Nesvacil, C. Kirisits, and M. Clausen, "Physical Fundamentals of Radio Oncology: Brachytherapy." Basic Seminar: Medical Physics VIII - Physical Fundamentals of Radio Oncology, Medical University of Vienna, 2019.

[7] E. B. Podgorsak *et al.*, "Radiation Oncology Physics: A Handbook for Teachers and Students," *Vienna: International Atomic Energy Agency*, pp. 123–271, 2005.

[8] Wikimedia Commons https://commons.wikimedia.org/wiki/File:Dose_Depth_Curves.svg, Feb. 2010. [accessed 23.07.2019].

[9] D. Dance, S. Christofides, A. Maidment, I. McLean, and K. Ng, "Diagnostic Radiology Physics: A Handbook for Teachers and Students," *International Atomic Energy Agency*, 2014.

[10] N. Nesvacil, Y. Seppenwoolde, P. Kuess, and M. Clausen, "Imaging & Setup for Radiation Oncology." Basic Seminar: Medical Physics VIII - Physical Fundamentals of Radio Oncology, Medical University of Vienna, 2019.

[11] F. M. Khan, J. P. Gibbons, and P. W. Sperduto, *Khan's Treatment Planning in Radiation Oncology*. Lippincott Williams & Wilkins, 4 ed., 2016.

[12] J. Seco and M. F. Spadea, "Imaging in particle therapy: State of the art and future perspective," *Acta Oncologica*, vol. 54, no. 9, pp. 1254–1258, 2015. PMID: 26329760.

[13] *ICRU Report 50. Prescribing, Recording and Reporting Photon Beam Therapy.* 1993.

[14] *ICRU Report 62. Prescribing, Recording and Reporting Photon Beam Therapy.* 1999. (Supplement to ICRU Report 50).

[15] F. M. Khan and J. P. Gibbons, *Khan's the Physics of Radiation Therapy.* Lippincott Williams & Wilkins, 2014.

[16] "Lung cancer." Eurostat `https://ec.europa.eu/eurostat/statistics-explained/index.php?title=Cancer_statistics_-_specific_cancers#Lung_cancer`, 2015. [accessed 31.07.2019].

[17] R. L. Siegel, K. D. Miller, and A. Jemal, "Cancer statistics, 2019," *CA: a cancer journal for clinicians*, vol. 69, no. 1, pp. 7–34, 2019.

[18] Globocan 2018, "Lung fact sheet." International Agency for Research on Cancer, World Health Organization, `https://gco.iarc.fr/today/data/factsheets/cancers/15-Lung-fact-sheet.pdf`, Mar. 2019. [accessed 05.09.2019].

[19] C. Bert and M. Durante, "Motion in radiotherapy: particle therapy," *Physics in Medicine & Biology*, vol. 56, no. 16, p. R113, 2011.

[20] P. Taylor, S. Kry, and D. S Followill, "Pencil Beam Algorithms Are Unsuitable for Proton Dose Calculations in Lung," *International Journal of Radiation Oncology*Biology*Physics*, vol. 99, pp. 750–756, Nov. 2017.

[21] K. Saladin, *Human Anatomy.* McGraw-Hill, 2 ed., 2008.

[22] H. Krieger, *Grundlagen der Strahlungsphysik und des Strahlenschutzes.* Springer, 5 ed., Mar. 2017.

[23] E. B. Podgorsak, "Radiation Physics for Medical Physicists," 2010.

[24] W. D. Newhauser and R. Zhang, "The physics of proton therapy," *Physics in Medicine and Biology*, vol. 60, pp. R155–R209, Mar. 2015.

[25] National Institutes of Standards and Technology `https://www.physics.nist.gov/PhysRefData/Star/Text/programs.html`. [accessed 10.08.2019].

[26] W. Demtröder, *Experimentalpysik 4: Kern-, Teilchen-, Astrophysik.* Springer-Verlag, 4 ed., 2014.

[27] J. Ziegler, "Stopping of energetic light ions in elemental matter," *Journal of applied physics*, vol. 85, no. 3, pp. 1249–1272, 1999.

[28] W. R. Leo, *Techniques for nuclear and particle physics experiments: a how-to approach.* Springer-Verlag, 2 ed., 1994.

[29] E. Pedroni, S. Scheib, T. Böhringer, A. Coray, M. Grossmann, S. Lin, and A. Lomax, "Experimental characterization and physical modelling of the dose distribution of scanned proton pencil beams," *Physics in Medicine and Biology*, vol. 50, pp. 541–561, Jan. 2005.

[30] M. Urie, M. Goitein, W. R. Holley, and G. T. Y. Chen, "Degradation of the Bragg peak due to inhomogeneities," *Physics in Medicine and Biology*, vol. 31, pp. 1–15, Jan. 1986.

[31] G. O. Sawakuchi, U. Titt, D. Mirkovic, and R. Mohan, "Density heterogeneities and the influence of multiple Coulomb and nuclear scatterings on the Bragg peak distal edge of proton therapy beams," *Physics in Medicine and Biology*, vol. 53, pp. 4605–4619, Aug. 2008.

[32] U. Schneider, E. Pedroni, and A. Lomax, "The calibration of CT Hounsfield units for radiotherapy treatment planning," *Physics in Medicine and Biology*, vol. 41, pp. 111–124, Jan. 1996.

[33] R. Zhang and W. D. Newhauser, "Calculation of water equivalent thickness of materials of arbitrary density, elemental composition and thickness in proton beam irradiation," *Physics in Medicine & Biology*, vol. 54, no. 6, p. 1383, 2009.

[34] B. Gottschalk, "Passive Beam Spreading in Proton Radiation Therapy (Draft 2004)," Oct. 2004.

[35] S. Goßner, *Grundlagen der Elektronik: Halbleiter, Bauelemente und Schaltungen; ein Lernbuch*. Shaker, 6 ed., 2008.

[36] Aspencore, Electronics Tutorials `https://www.electronics-tutorials.ws/diode/schottky-diode.html`. [accessed 08.09.2019].

[37] E. J. Hall and A. Giaccia, *Radiobiology for the Radiologist*. Philadelphia: Lippincott, Williams, and Wilkins Company, 7 ed., 2012.

[38] M. Durante, H. Paganetti, A. Pompos, S. F. Kry, X. Wu, and D. R. Grosshans, "Report of a National Cancer Institute special panel: Characterization of the physical parameters of particle beams for biological research," *Medical physics*, vol. 46, no. 2, pp. 37–52, 2019.

[39] W. Schneider, T. Bortfeld, and W. Schlegel, "Correlation between CT numbers and tissue parameters needed for Monte Carlo simulations of clinical dose distributions," *Physics in Medicine & Biology*, vol. 45, no. 2, p. 459, 2000.

[40] RaySearch Laboratories AB, *RayStation 7 Reference Manual*, 2017.

[41] PTW-Freiburg, Germany, *User Manual Bragg Peak Chambers Type 34070, 34073 and 34080*, 2009.

[42] PTW-Freiburg, Germany, *User Manual microDiamond Type 60019*, 2013.

[43] U. Titt, M. Sell, J. Unkelbach, M. Bangert, D. Mirkovic, U. Oelfke, and R. Mohan, "Degradation of proton depth dose distributions attributable to microstructures in lung-equivalent material," *Medical physics*, vol. 42, pp. 6425–6432, Nov. 2015.

[44] N. Kostiukhina, D. Georg, S. Rollet, P. Kuess, A. Sipaj, P. Andrzejewski, H. Furtado, I. Rausch, W. Lechner, E. Steiner, *et al.*, "Advanced Radiation DOSimetry phantom (ARDOS): a versatile breathing phantom for 4D radiation therapy and medical imaging," *Physics in Medicine & Biology*, vol. 62, no. 20, p. 8136, 2017.

[45] P. A. Webb, "Volume and Density Determinations for Particle Technologists," Jan. 2001.

[46] JGO, *Medical Physics Jour Fix.* MedAustron, Feb. 2016.

[47] T. P. Ringbæk, Y. Simeonov, M. Witt, R. Engenhart-Cabillic, G. Kraft, K. Zink, and U. Weber, "Modulation power of porous materials and usage as ripple filter in particle therapy," *Physics in Medicine and Biology*, vol. 62, pp. 2892–2909, Mar. 2017.

[48] M. Witt, "Modulationseffekte von Kohlenstoffionen bei der Bestrahlung von Lungen," Master's thesis, Technische Hochschule Hessen, 2014.

[49] K.-S. Baumann, M. Witt, U. Weber, R. Engenhart-Cabillic, and K. Zink, "An efficient method to predict and include Bragg curve degradation due to lung-equivalent materials in Monte Carlo codes by applying a density modulation," *Physics in Medicine and Biology*, vol. 62, pp. 3997–4016, Apr. 2017.

[50] T. Bortfeld, "An analytical approximation of the Bragg curve for therapeutic proton beams," *Medical Physics*, vol. 24, no. 12, pp. 2024–2033, 1997.

[51] V. Flatten, K.-S. Baumann, U. Weber, R. Engenhart-Cabillic, and K. Zink, "Quantification of the dependencies of the Bragg peak degradation due to lung tissue in proton therapy on a CT-based lung tumor phantom," *Physics in Medicine & Biology*, 2019.

[52] D. Markel, I. Levesque, J. Larkin, P. Léger, and I. El Naqa, "A 4D biomechanical lung phantom for joint segmentation/registration evaluation," *Physics in Medicine & Biology*, vol. 61, no. 19, p. 7012, 2016.

[53] R. Mayer, P. Liacouras, A. Thomas, M. Kang, L. Lin, and C. B. Simone, "3D printer generated thorax phantom with mobile tumor for radiation dosimetry," *Review of Scientific Instruments*, vol. 86, no. 7, p. 074301, 2015.

[54] H. Fuse, T. Fujisaki, R. Ikeda, and Z. Hakani, "Applicability of Lung Equivalent Phantom Using the Cork with Absorbed Water in Radiotherapeutic Dosimetry," *International Journal of Medical Physics, Clinical Engineering and Radiation Oncology*, vol. 7, no. 01, p. 27, 2018.

[55] B. Schaffner, E. Pedroni, and A. Lomax, "Dose calculation models for proton treatment planning using a dynamic beam delivery system: an attempt to include density heterogeneity effects in the analytical dose calculation," *Physics in Medicine & Biology*, vol. 44, no. 1, p. 27, 1999.

[56] S. España and H. Paganetti, "Uncertainties in planned dose due to the limited voxel size of the planning CT when treating lung tumors with proton therapy," *Physics in Medicine & Biology*, vol. 56, no. 13, p. 3843, 2011.

[57] K. R. Russell, E. Grusell, and A. Montelius, "Dose calculations in proton beams: range straggling corrections and energy scaling," *Physics in Medicine & Biology*, vol. 40, no. 6, p. 1031, 1995.

Acknowledgements

First of all, I want to thank Univ.-Prof. DI. Dr. Dietmar Georg for his supervision of this thesis. I am grateful for providing me with the opportunity to work at MedAustron and getting first hand experience with the particle accelerator and ion beam therapy.

Secondly, I owe my deepest gratitude to my co-supervisor Mag. Barbara Knäusl, PhD. Her support and talent was essential for the achieved quality of this thesis.

Moreover, I want to thank DI. Hermann Fuchs, PhD, Rubén Gonzalo Gleyzes, MSc, and Andreas Franz Resch, MSc for their support in the measurement sessions.

Additionally to the persons above, I would also like to thank Dr. Monika Clausen, DI. Gert Heilemann, PhD and Natalia Kostiukhina, MSc for helpful advises and fruitful discussions, especially during lunch and coffee breaks.

A special thanks and my deepest gratitude I want to express to my parents and family, who supported me during my studies and kept my spirit brightened up in dark times.

Statement of Originality

I declare that I have authored this thesis independently, that I have not used other than the declared sources / resources, and that I have explicitly marked all material which has been quoted either literally or by content from the used sources.

Vienna, on October 21, 2019

Signature